Complex network analysis of extreme precipitations in North America

by

Victor Abimbola Oladoja

B.Tech., Federal University of Technology, Akure, 2019

A THESIS

submitted in partial fulfillment of the requirements for the degree

MASTER OF SCIENCE

Department of Geology
College of Arts and Sciences

KANSAS STATE UNIVERSITY
Manhattan, Kansas

2024

Approved by:

Major Professor
Dr. Behzad Ghanbarian

Copyright

© Victor Oladoja 2024.

Abstract

Improving climate models for predicting water-related hazards such as floods and managing water resources depends on identifying the complex patterns of extreme precipitation events (EPEs). In this regard, we studied EPEs in North America using complex network analysis. We generated the EPEs network from the gauge-based daily precipitation dataset from the Climate Prediction Center database. The geographical grid points serve as the network's nodes, while the associations among them, captured using a non-linear method called event synchronization, represent the network's links. We determined the spatiotemporal patterns of the dependencies of EPEs through network measures such as degree centrality, mean geographical distance, betweenness centrality, clustering coefficient, and long-ranged directedness. We found hubs—locations important in propagating EPEs and teleconnections—in areas such as Montana, Wyoming, Alberta, and Saskatchewan in the summer and the West Coast and eastern North America in the winter. Our work demonstrated that EPEs are more spatially coherent during winter than summer across the continent. We identified certain locations in Utah, Colorado, South Dakota, northern Mexico, southeast British Columbia, and northern Quebec that play a crucial role in the long spatial propagation of EPEs from one region to another throughout the summer, while regions in the West Coast, southern Colorado, New Mexico, Wisconsin, central Alberta, etc., are dominant in the winter. Additionally, we uncovered atmospheric moisture pathways for EPEs in both seasons on the continent. Finally, we showed that EPEs networks are sensitive to τ_{max}, a parameter of the ES method. As such, it should be defined relative to the atmospheric phenomena of interest. The insights from this study revealed synchronization patterns of EPEs across North America and advanced our understanding of complex relationships and interdependencies between

topography and precipitation patterns. Further, analytics provided here can serve as a basis for improving the forecasting of hydrologic extremes and associated risks.

Table of Contents

List of Figures

List of Tables

Acknowledgements

Earning a master's degree is a journey, and this thesis would not have been possible without the support and guidance of many incredible people.

First and foremost, I would like to express my sincere gratitude to my major advisor, Dr. Behzad Ghanbarian. Your invaluable guidance, insightful feedback, and unwavering encouragement throughout this process were pivotal in shaping my research and keeping me motivated. I am deeply grateful for your expertise and patience.

I extend my sincere thanks to my thesis committee members, Dr. Matthew Kirk and Dr. Pascal Hitzler. Their insightful observations, encouraging guidance, and thoughtful critiques proved invaluable in shaping a more robust thesis.

I am particularly grateful to Dr. Tayeb Jamali for his unwavering support and insightful feedback throughout this journey. His expertise in complex network theory and computer programming proved invaluable in ensuring the accuracy and reliability of my findings. Professor Juergen Kurths also deserves my deep appreciation for his invaluable insights into the methodology and for his guidance in interpreting the results within the broader context of existing research. I am also grateful to my lab mates, Kehinde Bosikun and Connor Saari, for their collaboration on this research topic.

With deepest gratitude, I acknowledge the profound impact of my esteemed course instructors, Drs. Claudia Adam, Karin Goldberg, Lior Shamir, Gyuhyeong Goh, Matthew Kirk, and Behzad Ghanbarian. Their dedication to teaching has significantly shaped my academic journey.

I extend my heartfelt appreciation to Kansas State University for fostering an enriching academic environment and providing countless opportunities for growth and learning. My gratitude also extends to the Department of Geology and the K-State Graduate School for their generous financial support throughout my graduate studies.

Finally, I am immensely grateful to my friends, family, and colleagues for their unwavering emotional and intellectual support throughout this academic endeavor. Your encouragement and understanding have been invaluable.

Dedication

I dedicate this work to my incredible family: Samuel, Esther, Blessing, Victoria, and Vincent. Your constant love, encouragement, and unwavering support have been my foundation throughout this journey. Thank you for always believing in me.

Chapter 1 - Introduction

Extreme precipitation events (EPEs) can disrupt everyday activities and cause significant losses for individuals and communities. They can damage infrastructure, trigger landslides, increase flood risks, and affect agriculture and health (Kunkel et al., 1999; Trenberth et al., 2003). These impacts directly and indirectly affect the economy and society, reducing productivity, increasing costs, and creating social problems (Easterling et al., 2000; Nissen & Ulbrich, 2017). For instance, according to Newman & Noy (2023), storm-related damages cost the world economy more than $200 billion between 2000 and 2019. Extreme rainfalls are expected to become more frequent and intense due to climate change (Fischer & Knutti, 2016), which poses a significant challenge to adaptation and resilience. However, adverse impacts of EPEs can be mitigated by enhancing our understanding of EPEs systems and advancing their forecasts.

Identifying and detecting the organizing behaviors of EPEs and understanding the underlying mechanisms can improve their forecasts. Although many methods, such as empirical orthogonal functions and kriging in geo-statistics, have been developed to study spatiotemporal characteristics of vast space-time atmospheric datasets (Hannachi et al., 2007), they are limited in obtaining propagating features needed to nail down the physical mechanisms behind complex systems such as EPEs. They might also require additional parameters and covariance models (Sun et al., 2018). However, the complex network theory (CNT) approach, which emerged during the last two decades, has been successfully applied in studying climate systems without the abovementioned limits. While CNT is a relatively young field in need of further development, it has proven effective in uncovering complex patterns of climate parameter(s) at various scales by leveraging climate time series (Ludescher et al., 2021). Specifically, CNT has been used successfully to reveal spatial patterns of extreme weather events and teleconnections (Boers et al., 2013, 2015, 2019; Gupta et al., 2021; Konapala et al., 2022; T. Liu et al., 2023; Mondal et al., 2023).

In this paper, we examine the spatial distribution of EPEs and their synchronization patterns across North America. Studies on the complex spatial patterns of EPEs have been conducted at many scales, including country (Jamali et al., 2023a; Mondal et al., 2020), sub-country (Sun et al., 2018), and global levels (Boers et al., 2019); but, as far as we are aware, no research has been done on the continent of North America. However, convection processes like frontal, monsoonal, jet streams, and other synoptic-scale dynamics that function on sizes bigger than country but lower than global levels may cause EPEs. So, we apply CNT to determine the spatial structures of EPEs in North America. Past studies revealed that meteorological processes vary seasonally (Papalexiou & Koutsoyiannis, 2016; Yang & Wu, 2019; Yuan & Miller, 2002). We, therefore, construct a network for both summer and winter seasons to capture seasonal variations in the spatiotemporal configurations of North American EPEs. We unravel the complex and topological characteristics of EPEs networks and provide climatological interpretations through network measures, including degree centrality, clustering coefficient, mean geographical distance, betweenness centrality, long-ranged directedness, and community detection. We detect important geographic locations in the synchronizations of EPEs and teleconnections. Our analyses also reveal regions dominated by mid-latitude cyclones as well as pathways for moisture transport on the continent. We further explore the possible meteorological factors that could lead to the discovered patterns and their coherence on the continent.

1.1 Climate setting

Understanding the dominant atmospheric processes on the continent is essential for investigating extreme precipitation events. Here, we attempt to describe North America's principal atmospheric circulations. Atmospheric circulations over North America have important features such as the North American monsoon (NAM) (Adams & Comrie, 1997), atmospheric rivers (ARs) (Gershunov et al., 2017; Gimeno et al., 2014), orographic ascent (OA) (Houze, 2012; Viale et al., 2013), and frontal systems (FS) (Neiman et al., 2004; Viale et al., 2013) which have considerable impacts on precipitation patterns across the continent. NAM dominates during the summer, extending from northwest Mexico to the western United States (Adams & Comrie, 1997) and from the central United States to Canada (Liebmann et al., 2008a). It developed due to the temperature difference between the continent and the Pacific Ocean, which affects the transport of low-level jets from the ocean basin to the land and, if amplified, can result in extreme precipitations (Mechoso et al., 2012). ARs, on the other hand, transport large quantities of water vapor from the tropics to high latitudes through the lower troposphere and can persist for several days (Zhu & Newell, 1994). ARs, which carry as much water as the Amazon River upon landfall, are characterized by the occurrence of extreme precipitations and associated climate hazards. Hydroclimate on the west coast of North America is particularly sensitive to land-falling ARs in the winter, as they can significantly influence whether a year is wet or dry (Gershunov et al., 2017, 2019).

Chapter 2 - Material and methods

2.1 Data

We used the gridded gauge-based precipitation dataset provided by the National Oceanic and Atmospheric Administration (NOAA) Climate Protection Center (CPC). The CPC unified precipitation dataset is provided at a temporal resolution of mm/day and a spatial resolution of 0.5 by 0.5 degrees for global land areas from 1979 to the present (Xie et al., 2010). These precipitation analyses were derived from the Global Telecommunication System (GTS) daily summary files and the CPC unified daily gauge data across the contiguous United States (CONUS), Mexico, and South America. Since gauge stations are not uniformly distributed across the globe and their densities vary from region to region, the optimal interpolation method developed by Gandin (1965) was employed to generate daily precipitation analyses with biases below 0.01 for the needed spatial resolution (Chen et al., 2008). For our study, we extracted data for geographic grid points in North America for 30 years from 1991 to 2020 from the database, which is consistent with the 30-year normal.

2.2 Network Construction

2.2.1 Extreme Precipitation Events (EPEs)

Many definitions exist in the literature for extreme precipitation events (Liu et al., 2013). Here, however, we used the 95th percentile approach to define EPEs. At each season, for a given node, we considered any day with a precipitation value equal to or greater than the 95th percentile of all wet days on that node as an extreme precipitation event. It is important to note that a wet day is defined as any day with a precipitation magnitude exceeding 0 mm. As a result, extreme events are local to each node. An EPEs time series, simply referred to as an event series, is then constructed by assigning a value of one to the days featuring extreme events and zeros to all other days. Following Boers et al. (2019), consecutive extreme events are considered as a single extreme event only on the first occurrence. Next, we generated seasonal EPEs networks from the event series using the methods described hereafter.

2.2.2 EPEs synchronization

We uncovered pairwise dependencies among North American nodes using the event synchronization (ES) approach. To quantify the degree of synchronization between two univariate time series, Quiroga et al. (2002) created the ES approach to count the number of quasi-simultaneous appearances of events in these series.

Let $t^i_{1,\ldots,m}$ and $t^j_{1,\ldots,n}$ be event series at nodes *i* and *j*, respectively. The lengths of the series at these nodes are, accordingly, *m* and *n*. $ES^{i,j}$ determines the degree of associable events between nodes *i* and *j* by counting the number of temporal delays $\Delta^{i,j}_{m,n}$ that satisfy the following conditions: (1) $\left|\Delta^{i,j}_{m,n}\right| < \tau^{i,j}_{m,n}$ (local time scale) and (2) $\left|\Delta^{i,j}_{m,n}\right| \leq \tau_{max}$. The atmospheric processes that cause EPEs run from a few hours to a few days. Consequently, a constant τ_{max} (e.g., 10 days) is used to bind temporal delay between events to prevent unreasonable synchronization between them (Boers et al., 2014, 2019). The definitions for $\Delta^{i,j}_{m,n}$ and $\tau^{i,j}_{m,n}$ are given as follows.

$$\Delta^{i,j}_{m,n} = t^j_n - t^i_m \tag{1}$$

$$\tau^{i,j}_{m,n} = \frac{1}{2} \times min\left\{\Delta^{i,i}_{m,m-1}\,,\ \Delta^{i,i}_{m,m+1}, \Delta^{j,j}_{n,n-1}, \Delta^{j,j}_{n,n+1}\right\} \tag{2}$$

The local time scale $\tau^{i,j}_{m,n}$ is dynamic since it depends on events. Hence, ES works better for events-based networks than the correlation approach (Meng et al., 2018). We analyzed how sensitive EPEs networks are to τ_{max}, which is the maximum delay allowed between two events on different nodes before they could be deemed synchronous. Results for τ_{max} = 0 and 10 day(s) are largely presented here. Supplementary materials contain information regarding τ_{max} = 1, 2, 4, 6, 20 days.

2.2.3 Significance test and Adjacency matrix

The adjacency matrix gives information on the presence or absence of links between nodes in a network. The empirical values for the degrees of synchronization derived from ES have no information on their statistical significance. The straightforward method for forming links between nodes is by using a common threshold (Boers et al., 2013, 2015; Mondal et al., 2020, 2023; Sun et al., 2018). However, sometimes, this approach fails to account for potential biases that might arise from the variations in the number of events present in each node's time series. The null model method is an alternative and better approach that addresses such biases (Boers et al., 2019). For a pair of event series with a determined ES value, this method uses a set of pairs of shuffled event series to find the statistical significance of the ES value. Given two nodes, *i* and *j*, we assessed the statistical significance of the degree of synchronization $ES^{i,j}$, between them by simulating a null model distribution. We generated two shuffled event series of equal length for nodes i and j by randomly shuffling $t^{i}_{1,\ldots,m}$ and $t^{j}_{1,\ldots,n}$, respectively, 3000 times. On each iteration, ES was calculated and added to the model distribution. Using the 99.5th percentile of the null model distribution as the significance threshold, a link is placed between nodes *i* and *j* if $ES^{i,j}$ is greater than or equal to the threshold; otherwise, no link is placed. This ensures that the probability of having a link purely by chance is 0.005. The potential biases due to event rates are avoided through the null-model distribution. Lastly, links between nodes are represented with 1 on the adjacency matrix.

2.3 Network measures

Network measures are important for identifying the spatial patterns in a complex system such as the EPEs system. We give the definitions of various measures estimated in this work and the climatological inferences they could provide.

2.3.1 Degree centrality (DC)

The degree centrality of a node measures the importance of a node in a network based on the number of connections it has to other nodes. Formally, the degree k_i of node *i* is the number of nodes adjacent or neighbor to it. In the context of the EPEs network, degree indicates the amount of association between EPEs at one grid point with those occurring at other grid points. Nodes with high degrees are called hubs. In the EPEs network, hubs can be locations that are critical to extreme events propagation and, in some cases, teleconnections.

$$k_i = \sum_{j=1}^{N} A_{(i,j)} \tag{3}$$

2.3.2 Mean geographical distance (MGD)

MGD is a simple but powerful network measure that captures the arithmetic mean of the geographical distances between a node and its neighbors. For an EPEs network, MGD basically shows whether a location exhibits similar patterns of extreme precipitation with neighboring areas or those situated far away, on average. This node-based measure is thus defined as follows.

$$MGD_i = \frac{1}{k_i} \sum_{j=1}^{n} D_{(i,j)} A_{(i,j)} \tag{4}$$

$D_{(i,j)}$ is the geographical distance between nodes *i* and j. Places with high MGD are very likely to be involved in extreme events teleconnection, whereas places with low MGD will only be influential within their local geographical region.

2.3.3 Clustering coefficient (CC)

The clustering coefficient (CC) of node i, denoted by, C_i captures the degree to which the neighbors of node i are connected to one another. In simple terms, it gives information on how many nodes sharing links with a specific node are connected to one another. On two extreme ends, if a region contains nodes with low CC estimates, such region may lack spatial coherency in the occurrence of EPEs. Otherwise, if every node is connected to every other node in a region, then EPEs behavior in one grid cell will reflect extreme events behaviors in all grid locations within the region. That is, the region will exhibit a very high EPEs spatial coherency. In other words, CC informs of the network's local link density or local features. C_i is given given by:

$$C_i = \frac{2L_i}{\mathrm{k}(\mathrm{k}-1)} \tag{4}$$

where L_i represents the number of links among k neighbors of node i. C_i is between 0 (no connections among neighbors of the ith node) and 1 (all neighbors of the ith node are connected to one another).

2.3.4 Betweenness centrality (BC)

Another measure of a node’s importance is the betweenness centrality (BC). Compared to degree centrality, which measures the importance of a node in terms of the number of its neighbors, betweenness centrality prioritizes the node's position in a network. It determines how pivotal a node is in propagating information throughout a network by considering the number of paths that pass through it. A path from node v_s to node v_t is defined as the length of a walk between them using distinct nodes. Here, we use the normalized betweenness centrality, which is defined as follows.

$$C_{nb}(v_i) = \frac{2\sum_{v_s \neq v_i \neq v_t} \frac{\sigma_{st}(v_i)}{\sigma_{st}}}{(N-1)(N-2)} \tag{6}$$

Where σ_{st} is the number of shortest paths between nodes v_s and v_t and $\sigma_{st}(v_i)$ is the number of σ_{st} that passes through node v_i. $C_b(v_i)$ is normalized by $\frac{(N-1)(N-2)}{2}$, which is the maximum centrality score if all pairs of nodes are connected and all of them pass through Where σ_{st} is the number of shortest paths between nodes v_s and v_t and $\sigma_{st}(v_i)$ is the number of σ_{st} that passes through node v_i. $C_b(v_i)$ is normalized by $\frac{(N-1)(N-2)}{2}$, which is the maximum centrality score if all pairs of nodes are connected and all of them pass through node v_i. We refer interested readers to Ma & Tang (2021) for comprehensive details on the terms involved in estimating betweenness centrality.

2.3.5 Long-ranged directedness (LRD)

LRD was introduced by Boers et al. (2013) to capture the strength of a grid location in transporting moisture across large spatial distances. It is derived from the combination of the normalized values of MGD (NMGD), CC (NCC), and BC (NBC), which is stated below:

$$LRD = \frac{1}{2}NMGD + \frac{1}{2}NBC - NCC \tag{7}$$

LRD is particularly suitable for EPEs studies because it could reveal water vapor transport routes. For example, regions with high LRD values, as per its definition, will be highly dynamic and involved in transporting moisture over large spatial scales. However, locally extensive contiguous processes such as mesoscale convective systems will most likely dominate regions with low LRD values resulting from high CC, low MGD, and low BC. They will have little or no long-range impacts.

2.3.6 Community detection (CD)

Community detection is a type of clustering approach that can be used to detect communities inherent to a network. inherent to a network. It involves partitioning the network into subgroups that contain densely connected nodes with similar properties. Each node belongs to one and only one community, with nodes belonging to different communities being sparsely connected. By this, we combined community detection with the network measures discussed earlier to understand the spatial structure of covariation regions. There are many algorithms for finding community structures in networks with different drawbacks. In this study, we used the walktrap algorithm (Pons & Latapy, 2005) to subdivide the networks into communities. We also tried the Louvain algorithm (De Meo et al., 2011) and the Leiden algorithm (Traag et al., 2019) but the walktrap algorithm worked best. Interested readers may check the referenced works for further explanations.

2.4 Spatial significance of network measures

An EPEs network is a specific type of embedded network, where, in this context, it is embedded on the Earth's surface. Hence, the geographical location of a node (grid point) within an EPEs network can impact the accuracy of the network measure associated with that node. To elaborate, the nodes near the boundary of a spatially confined network, such as those on the West Coast of the United States, are likely to have connections with nodes located outside the North American continent. However, this is impossible, as we did not consider the Pacific Ocean when constructing our networks, which might introduce errors in the estimated network measures near the boundary. This effect is termed the boundary/spatial effect, and we corrected it following Rheinwalt et al. (2012). We normalize each measure at each node by dividing the original estimated value by the expectation value obtained through a set of surrogated versions of the original EPEs network. We achieved expectation values by generating 1000-surrogated networks. Readers may consult Rheinwalt et al. (2012) and Boers et al. (2013) for further explanations.

Chapter 3 - Result and Discussion

3.1 Precipitation Data Analysis

Here, we present our findings for the daily average precipitation from 1991 to 2020 across the North American continent for the JJA and DJF seasons. Many regions of the continent experience an average precipitation of less than 6 mm/day in both seasons. Places below latitude 30^0N receive the highest amount of rainfall in JJA, reaching up to 12mm/day, as depicted in Fig. 1(a). Eastern North America (NA), including eastern United States of America (USA) and southeast Canada, receives precipitation ranging from 4.5 to 9.0 mm/day precipitation in summer (see Fig. 1(a)). However, during the DJF season, western NA receives the highest precipitation, exceeding 7 mm/day (see Fig. 1(b)). The southeast USA receives moderate precipitation ranging from 3 to 6 mm/day. These results agree with earlier studies showing that NAM from the Gulf of Mexico dominates in the JJA season (Adams & Comrie, 1997), while ARs from the Pacific Ocean dominate in the DJF season (Gershunov et al., 2017, 2019; Gimeno et al., 2014).

The thresholds used to identify EPEs are displayed in Figure 1(c) and (d). We locally define EPEs thresholds for two reasons. Firstly, a precipitation event in a particular location is considered extreme when it is compared to the historical precipitation patterns observed in that specific location. Secondly, various geographical and climate factors can cause significant spatiotemporal variations in extreme events (B. Liu et al., 2013). The regions in southeast Texas, Midwest, and southern NA have the highest thresholds in the summer (see Fig 1(c)). Except for the southern region of the continent in DJF, there exist similarities between each season's average and threshold maps. The winter threshold pattern observed in the contiguous United States (CONUS) depicted in Fig. 1(d) is consistent with the result presented in Fig. 3 of Shrestha et al. (2013). The authors used meteorological station data from 206 cities obtained from the National Climatic Data Center to generate a map of the 95th percentile precipitation for the 1973-2010 period. In addition, the spatial patterns observed in CONUS shown in Fig. 1(c) and (d) are consistent with the 99th percentile maps reported by Dickinson et al. (2021) for 14-day extreme-event windows of precipitation in CONUS derived using data from 1915-2018 (see their Fig. 3). Figures 1(e) and (f) give the EPEs number per node. As mentioned, when generating event series from precipitation time series, consecutive events on a node are regarded as a single event, with only the first day of occurrence counted as EPE. Therefore, the number of EPEs varies between nodes. Figure 1(e) shows that the number of EPEs follows the same pattern as daily average precipitation in JJA. Our result is consistent with that of Jamali et al. (2023), who analyzed this property for the period spanning 1981 to 2020 using data from the same database.

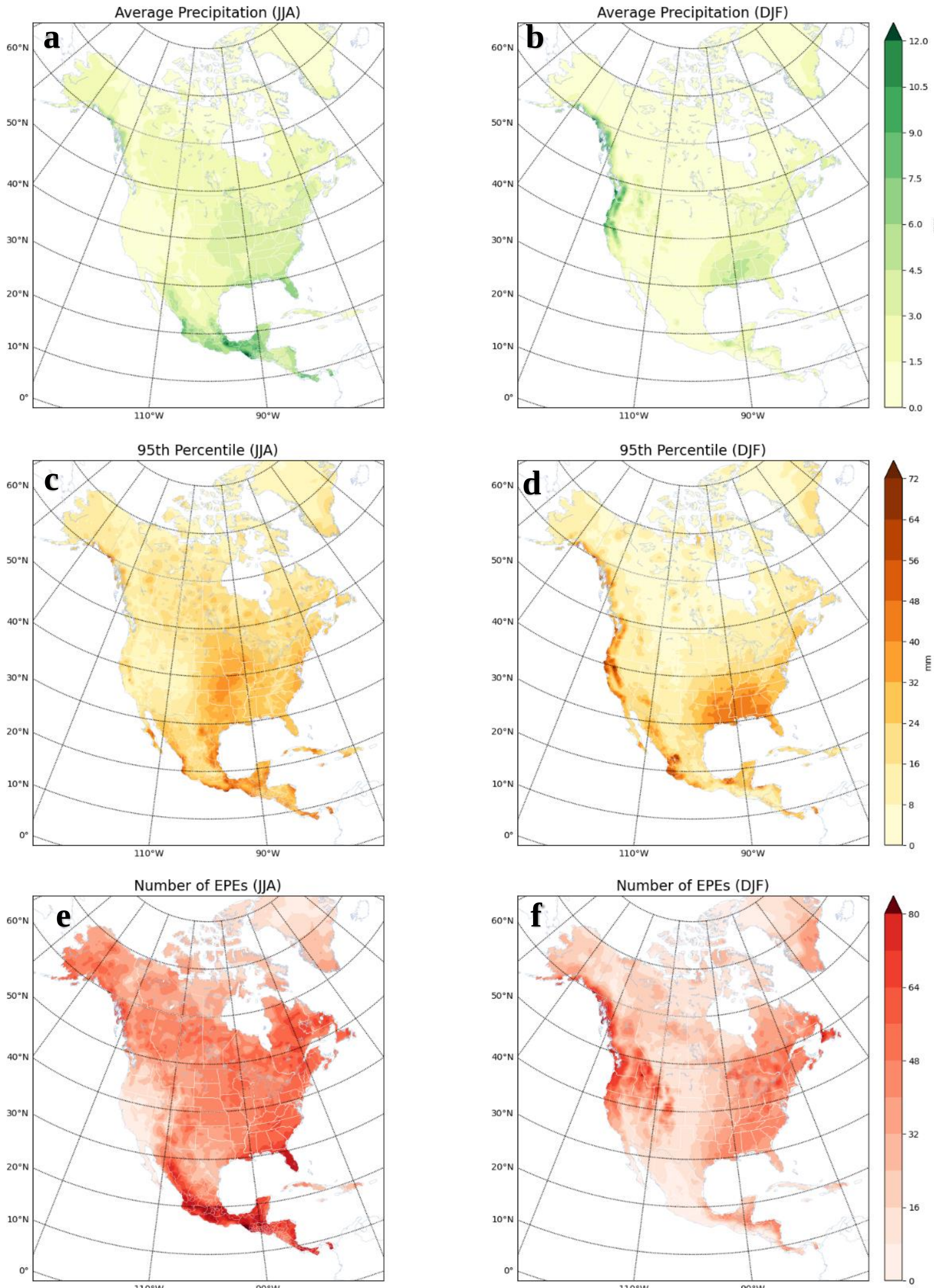

Figure 1. The top-level maps show the daily average precipitation, the middle-level maps show the values of the 95th percentile, and the bottom-level map shows the number of EPEs at each node for the period from 1991 to 2020. The JJA season is on the left column, while the DJF season is on the right. The same color bar range is used in each row to facilitate comparison between the two seasons.

In DJF, nodes with the highest number of EPEs are located within latitudes 30^0N and 60^0N, with regions on the continent's west coast having the highest EPEs (Fig. 1(f)). Regions in the Central Lowlands, east coast of CONUS, and extending to southeast Canada have moderate to high EPEs in the winter.

3.2 Network measures

In what follows, we will present the results obtained for EPEs networks during the summer and winter seasons. Readers should note that, apart from MGD, all measures were corrected for spatial effects following the approach described in section 2.4. We did not correct MGD for spatial effects because it contains information on average of geographical distances between a node and all nodes connected to it within the North American continent. We will present and discuss results for different τ_{max} to determine how the roles of nodes change under different temporal scales. As mentioned earlier, τ_{max} is the maximum delay allowed between two events on different nodes before they can be deemed synchronous. In other words, τ_{max} enables the differentiation of EPEs patterns caused by atmospheric phenomena operating on distinct time scales.

Figure 2(a) and (b) show degree centrality (DC) in the JJA season at $\tau_{max} =$ 0 and 10 days. In Fig. 2(a), we observed regions with high DC largely within latitudes 40^0N and 60^0N. Recall that, as per the definition of DC in Eq. (3), a high-degree location indicates that EPEs in this location occur synchronously with many other locations on the continent. The northern Great Plains region of North America, which includes states like Montana, Wyoming, and Idaho in CONUS and parts of Alberta and Saskatchewan in Canada, are hubs in the JJA EPEs network. In addition, some regions in Nunavut and Quebec in Canada and Alaska have high DC estimates. Our result is consistent with those of Mondal et al. (2020) and Jamali et al. (2023). Figure 2 (a) is comparable to Fig. 2(a) of Mondal et al. (2020) and Fig. 4(a) of Jamali et al. (2023), whose works both analyzed EPEs for CONUS. Both authors used precipitation data from the CPC database to construct EPEs networks at $\tau_{max} = 3$ and 0 days, respectively. Mondal et al. (2020) considered the period from 1979 to 2017, while Jamali et al. (2023) focused on the timeframe spanning from 1991 to 2020. Our result exhibits greater consistency with that of Jamali et al. (2023) than Mondal et al. (2020), as we observed higher DCs in Montana than in the northeastern United States. This similarity is probably because we analyzed the same period as Jamali et al. (2023). From the JJA EPEs networks constructed using different τ_{max}, we observed that the Montana and Alberta regions remain highly connected until $\tau_{max} =$ 6 days in the summer (Please check the supplementary material for more details).

In contrast to the summer season, during winter, with τ_{max} set to 0 days and within latitudes 30^0N and 55^0N, hubs in the EPEs network shifted toward the eastern parts of the continent (Fig. 2(c)). At $\tau_{max} = 10$ days (Fig. 2(d)), this region extends from northeast Texas to Florida to southeast Canada. Regions in the western parts of the Rocky Mountains are moderately connected at $\tau_{max} = 0$,1 and 2 days.

However, they become highly connected at $\tau_{max} = 4$ days and remain even at $\tau_{max} = 20$ days (Please check the supplementary materials for maps at $\tau_{max} = 1$,2,4,6, and 20 days). Our finding is similar to Banerjee et al. (2023), who used the edit distance method and ERA5 reanalysis data to construct CONUS extreme winter precipitation network for the period 1980-2020 (see their Fig. 4a), and Jamali et al. (2023) (see their Fig. 4b). Vallejo-Bernal et al. (2023) attributed strong connections that emerged at $\tau_{max} = 4$ days to land-falling ARs.

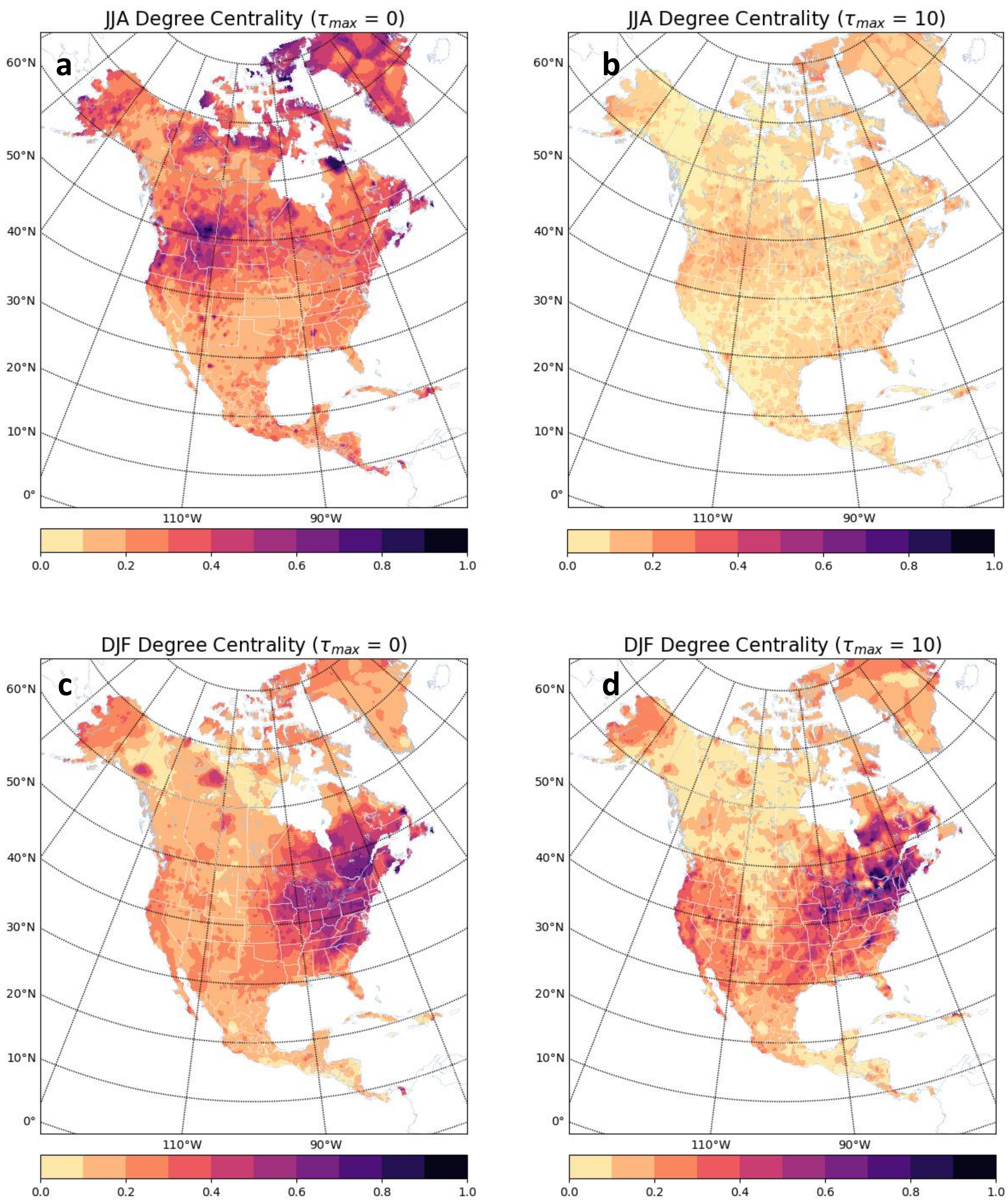

Figure 2. The upper maps show degree centrality for the summer season, while the lower ones are for winter. Degree centrality maps for $\tau_{max} = 0$ days are on the left column, and those for $\tau_{max} = 10$ days are on the right.

Tables 1 and 2 show that generating EPEs networks using the ES method is sensitive to the choice of τ_{max}. We found that none of the links' distributions at various τ_{max} for both JJA and

DJF seasons exhibit identical distributions, as determined by the Kolmogorov-Smirnov test (KS test) (Massey, 1951). Further, we observed that the average number of links per node is different at various τ_{max} for both seasons using the T-test (see Table 3 and 4 in the appendix).

The mean geographical distance (MGD) network measure defined in Eq. (4) demonstrates the average spatial distance over which a node synchronizes with other linked nodes. Hence, high MGD regions indicate that nodes within these regions are involved in teleconnections. The North American maps of MGD for both DJF and JJA seasons are shown in Fig. 3 (a)-(d). MGD ranged from 255 to 6446 km at $\tau_{max} = 0$ for the summer season and 50 to 5760 km at $\tau_{max} = 10$. While in the winter season, MGD ranged from 226 to 6059 km and 50 to 5703 km at $\tau_{max} = 0$ and 10 days, respectively. On average, there are longer teleconnections happening in JJA than in DJF season across the continent. The maximum MGDs for both seasons at $\tau_{max} = 10$ are lower than at 0, probably due to the definition of the ES method in section 2.2.2. For instance, for two nodes *i* and j, if the time delay between t_{m1}^{i} and t_{m2}^{i} is less than the delay between t_{m1}^{i} and t_{n1}^{j}, $t_{m1}^{i}$and t_{n1}^{j} will not be synced.

Table 1. P-values from KS tests for DC distributions at different τ_{max} in the summer season. The null hypothesis is that collections of DC at two τ_{max} are drawn from the same probability distribution at a 0.05 significant level.

τ_{max} \ τ_{max}	1	2	4	6	10	20
0	< 0.0001	< 0.0001	< 0.0001	0.0000	0.0000	0.0000
1		< 0.0001	< 0.0001	0.0000	0.0000	0.0000
2			< 0.0001	0.0000	0.0000	0.0000
4				0.0000	0.0000	0.0000
6					0.0000	0.0000
10						0.0000

Table 2. P-values from KS tests for DC distributions at different τ_{max} in the winter season. Table 2 follows the same assumptions as Table 1.

τ_{max} \ τ_{max}	1	2	4	6	10	20
0	< 0.0001	< 0.0001	< 0.0001	< 0.0001	< 0.0001	0.0000
1		< 0.0001	< 0.0001	< 0.0001	< 0.0001	< 0.0001
2			0.0000	0.0000	< 0.0001	< 0.0001
4				< 0.0001	< 0.0001	0.0000
6					< 0.0001	< 0.0001
10						< 0.0001

In the summer, at $\tau_{max} = 0$, a narrow rope-like region extending from tropical North America to Mexico, terminating in eastern Arizona and western New Mexico, CONUS is involved in geographically distant connections. They have MDG values above 3200 km (Fig. 3(a)). Some regions in the Appalachian Highlands also have high MGD. During the JJA season, on average, large parts of the continent are connected to other parts at 600 – 1800 km. Meanwhile, the MGD pattern is like the DJF degree pattern at $\tau_{max} = 0$ days in winter. The tropics, southwestern Canada, Appalachian Highlands, and Mounts McKenzie regions in Alaska are places with moderate to high MGD values, greater than 2500 km distance. Figures 3 (a) to (d) show that nodes with moderate to high MGD are less spatially distributed in the summer compared to the winter season. This phenomenon is attributed to the occurrence of precipitation-causing larger atmospheric systems in the winter.

Here, we will focus on the crossover distance between EPEs produced by regional weather systems and large-scale teleconnections such as synoptic-scale atmospheric circulations. Boers et al. (2019) studied global patterns of extreme rainfall teleconnections using the complex network approach. The authors examined teleconnections by estimating the geographical distances of all links and analyzing their corresponding distribution. Jamali et al. (2023) carried out a similar investigation at the sub-continental scale. Likewise, our study follows a comparable approach. Since teleconnections are climate anomalies that are related to each other over large distances (Feldstein & Franzke, 2017), especially at the synoptic scale and above, we used distance histogram to find the crossover between regional EPEs systems and those at the synoptic scale and above, i.e., large scale. Figures 4(a) to (d) show the log-log histogram plots for geographical distance distributions for JJA and DJF seasons at $\tau_{max} = 0$ and 10 days. We find clear crossovers at $\tau_{max} = 0$ and 10 days for the summer at 2750 and 3150 km, respectively.

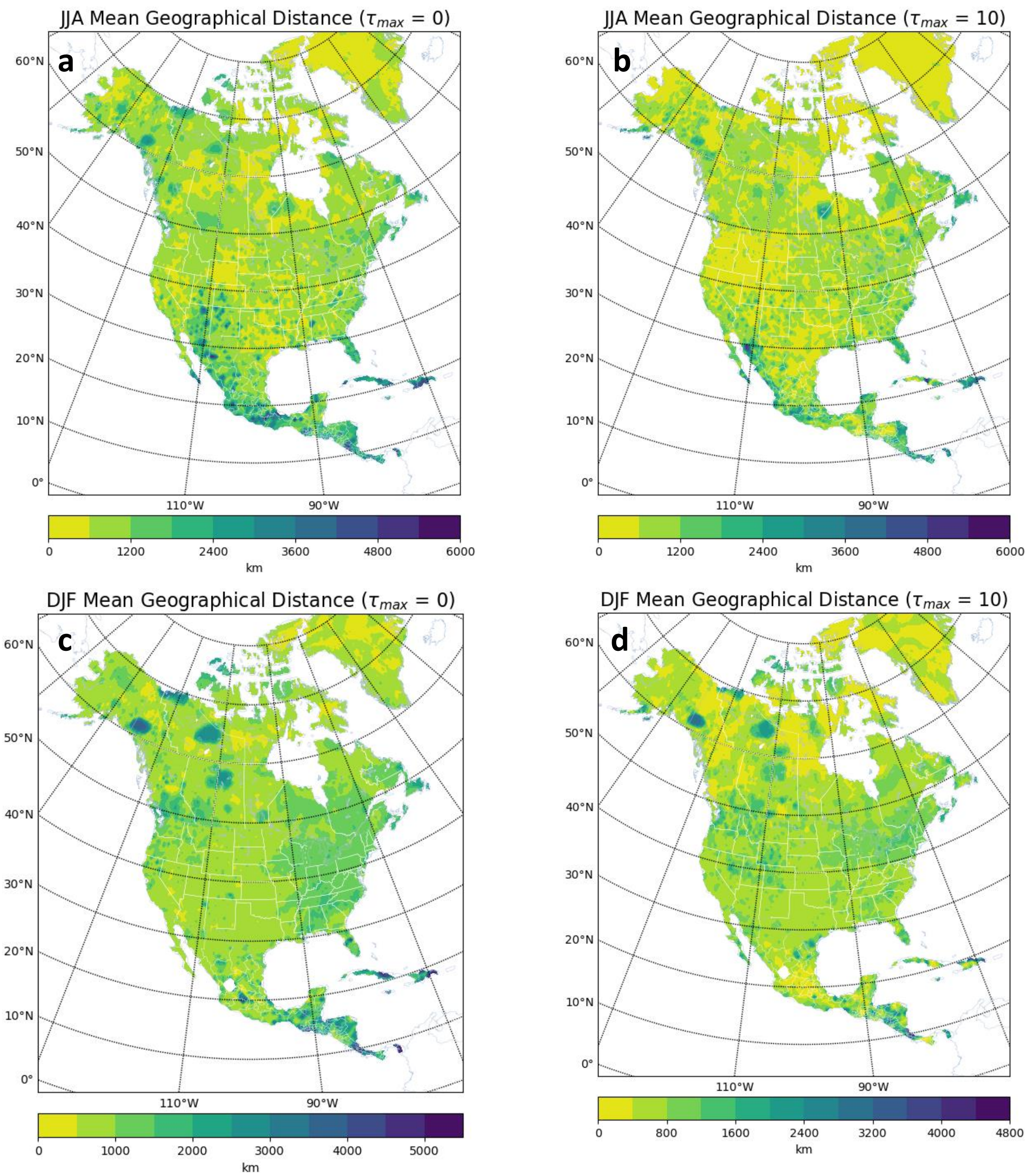

Figure 3. The top maps show the mean geographical distance for the summer season, while those at the bottom display the same for winter. The mean geographical distance maps for $\boldsymbol{\tau_{max}} = 0$ days are showcased in the left column, whereas those corresponding to $\boldsymbol{\tau_{max}} = 10$ days are depicted in the right column.

However, the crossovers in DJF seasons are 2200 and 2650 km, respectively. Raising the value of τ_{max} shifts the crossover to the right because higher τ_{max} captures precipitationproducing weather phenomena operating over a broader spatial range. The crossovers at $\tau_{max} = 0$ in both JJA and DJF, are higher than those obtained by Jamali et al. (2023) at the CONUS scale. They found a crossover around 2600 and 2000 km for the summer and winter seasons, respectively. This is because we used the same data set but on a bigger scale. The regime shifts witnessed at a crossover represent a transition from EPEs synchronization caused by regional precipitation systems (e.g., mesoscale convective systems) to large-scale systems (e.g., synoptic-scale Rossy waves and cyclones). We need to investigate further, why the crossover in winter is less than in summer.

The clustering coefficient (CC) is important for examining the spatial coherence of EPEs systems. A node with a high CC value has many interconnectivities among its neighbors (Mondal et al., 2020). In the summer, many parts of the continent have low to very low CC at both $\tau_{max} = 0$ and 10 days (Fig. 5(a) and (b)). However, some regions in the Caribbean, such as Cuba, Haiti, and Jamaica, and regions close to water bodies, such as Hudson Bay in Canada, have moderate CC values of around 0.5 at $\tau_{max} = 0$ days. Studies have shown that the Caribbean is prone to hurricanes in the wet season (June to November) (Jones et al., 2016; Taylor et al., 2002), which explains the coherence in EPEs during the JJA. At $\tau_{max} = 2$ days (please see Fig. 4(b) in the supplementary information section), we observed moderate CC in regions in the west of Cascade and Sierra Nevada Mountains, northeast Montana, and some regions in Texas, in addition to those identified at $\tau_{max} = 0$.

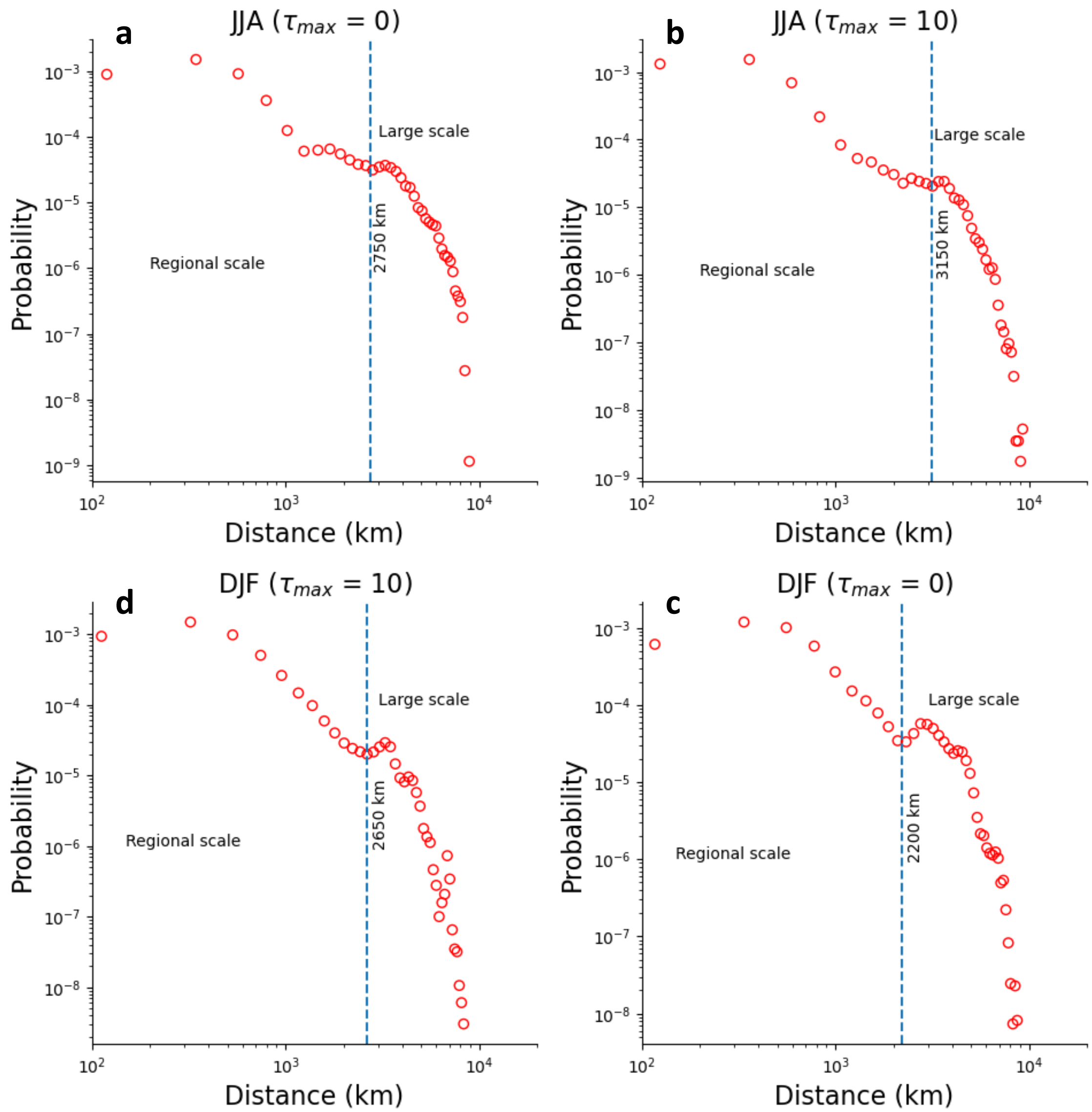

Figure 4. The histogram graphs for distance distribution of EPEs synchronizations for JJA and DJF seasons. Crossover points at $\boldsymbol{\tau_{max}} = 0$ and 10 days (dashed blue lines) for JJA are displayed on the top plots (93.7% and 95.7% of the links are from regional weather systems (RWS), respectively). While those for the DJF seasons are shown on the bottom plots (links from RWS are respectively, 89.7% and 96.3%).

Our result at $\tau_{max} = 2$ (see supplementary information section Fig. 15(c)) is consistent with Fig. 2(c) of Mondal et al. (2020) in regions such as Texas, southern California, Great Plains, Montana, and New York.

Meanwhile, EPEs are more spatially coherent in the winter at $\tau_{max} = 2$. Regions with moderate to high CC include the Midwest, CONUS eastern and western coast, and southeast Canada. Some regions immediately east of the Sierra Nevada Mountains in the Great Basin have low CC (Fig. 5c). Our work agrees with Miller and Goodrich (2007), who studied the regional coherence of precipitation in the Pacific Northwest during the winter season using principal component analysis. We find sub-region variability in EPEs in the Pacific Northwest, with some parts having low CC and others moderate CC. At $\tau_{max} = 10$ days, however, most parts of the continent exhibit low CC. This shows that when considering synchronizations between extreme events that happen within a period of 10 days or less of one another, there is spatial variability in EPEs across North America in the winter.

We will next focus on betweenness centrality (BC), which accounts for how important a node/place is in transferring EPEs from one region to another on the continent. In other words, BC, as defined in Eq. (6), gives information on the influence of a grid point in the long-range spatial propagation of EPEs (Boers et al., 2013). Figures 6(a) - (d) show BC's North American spatial patterns at $\tau_{max} = 0$ and 10 days for JJA and DJF seasons, respectively. It is important to note that BC values are often small with a very wide range, and theoretically, it is possible to have a BC estimate of 0. Therefore, rather than presenting the results using BC values, we used log(Betweenness Centrality + 1), which provides better visualization. The logarithmic scale helps to display data with a wide range better and shifting BC by unity helps to avoid undefined values when BC is zero. In the summer season, we observe high BC in many parts of the continent at $\tau_{max} = 0$.

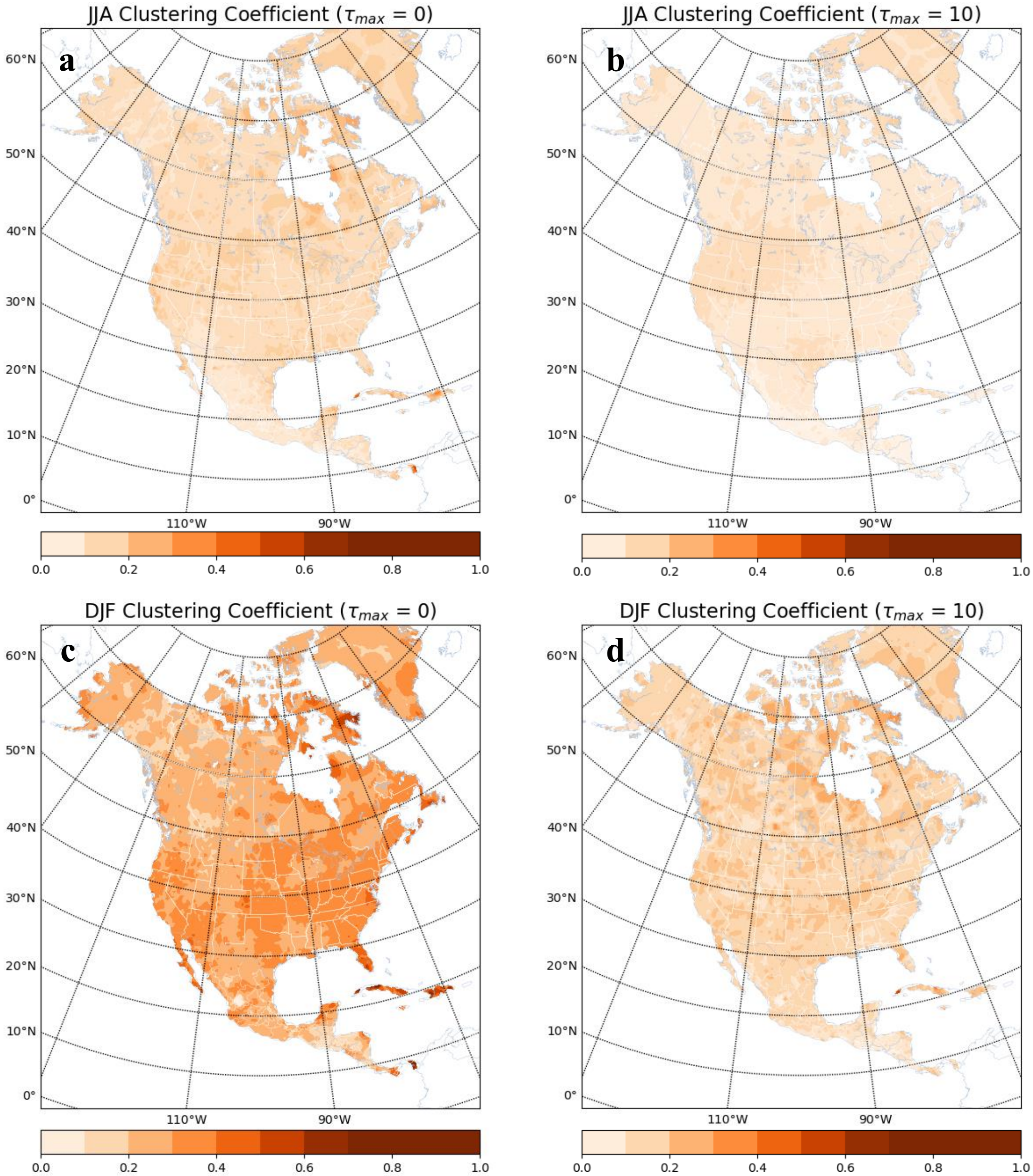

Figure 5. The upper maps show the clustering coefficient for the summer season, while the lower ones are for the winter. The clustering coefficient maps at $\boldsymbol{\tau_{max}} = 0$ days are in the left column, and those for $\boldsymbol{\tau_{max}} = 10$ days are in the right.

In the CONUS, these places include some regions in Utah, Colorado, Arizona, New Mexico, southern Texas, northeast Tennessee, eastern South Dakota, New York, and southwest Virginia. Some areas in tropical Mexico and northern Mexico exhibit high BC (Fig. 6(a)).

In Canada, places in southern Alberta, northern Quebec, and southeast British Columbia are also important in the long-range spatial propagation of EPEs. Our result is consistent with that of Mondal et al. (2020) in Colorado, New York, Maine, and California, who studied summer extreme precipitation in CONUS. At $\tau_{max} = 10$ days, the strength of these places in broadcasting EPEs decreased significantly (Fig. 6(b)). However, we observed smaller BC values in Florida than they reported (see their Fig. 2(a)). Fig. 6(c) displays the BC spatial pattern in DJF at $\tau_{max} = 0$ days. Regions that are significant in water-vapor transport in the winter include areas on the west coast of North America and the Gulf of Alaska, southern Colorado, New Mexico, southern Texas, northeast Mexico, Wisconsin, northwest Saskatchewan, central Alberta, etc. We have similar results as Banerjee et al. (2023) in regions of northwest CONUS, Wisconsin, and the northeast coast of CONUS; please refer to their Fig. 4(b) for comparison. They studied CONUS extreme precipitation for the winter season using the edit distance approach. Comparing Fig. 6(c) to 6(d) shows that the northeastern CONUS becomes increasingly important in moving atmospheric moisture over a longer temporal range in the winter.

One of the major foci of our work is to detect transport routes for atmospheric moisture-producing EPEs. Long-ranged directedness (LRD), a composite measure derived from MGD, CC, and BC, is an effective tool for identifying such routes (see the definition of LRD in Eq. (7)). In the summer season when considering EPEs happening within a day of each other for synchronization, we observed high LRD in a narrow region starting at the southwestern slope of Sierra Madre Oriental and extending to Arizona, New Mexico, Utah, and Colorado (Fig. 7(a)). This pattern aligns with the moisture transport routes reported in the literature for the North American Monsoon (NAM) system (Barlow et al., 1998; Douglas et al., 1993).

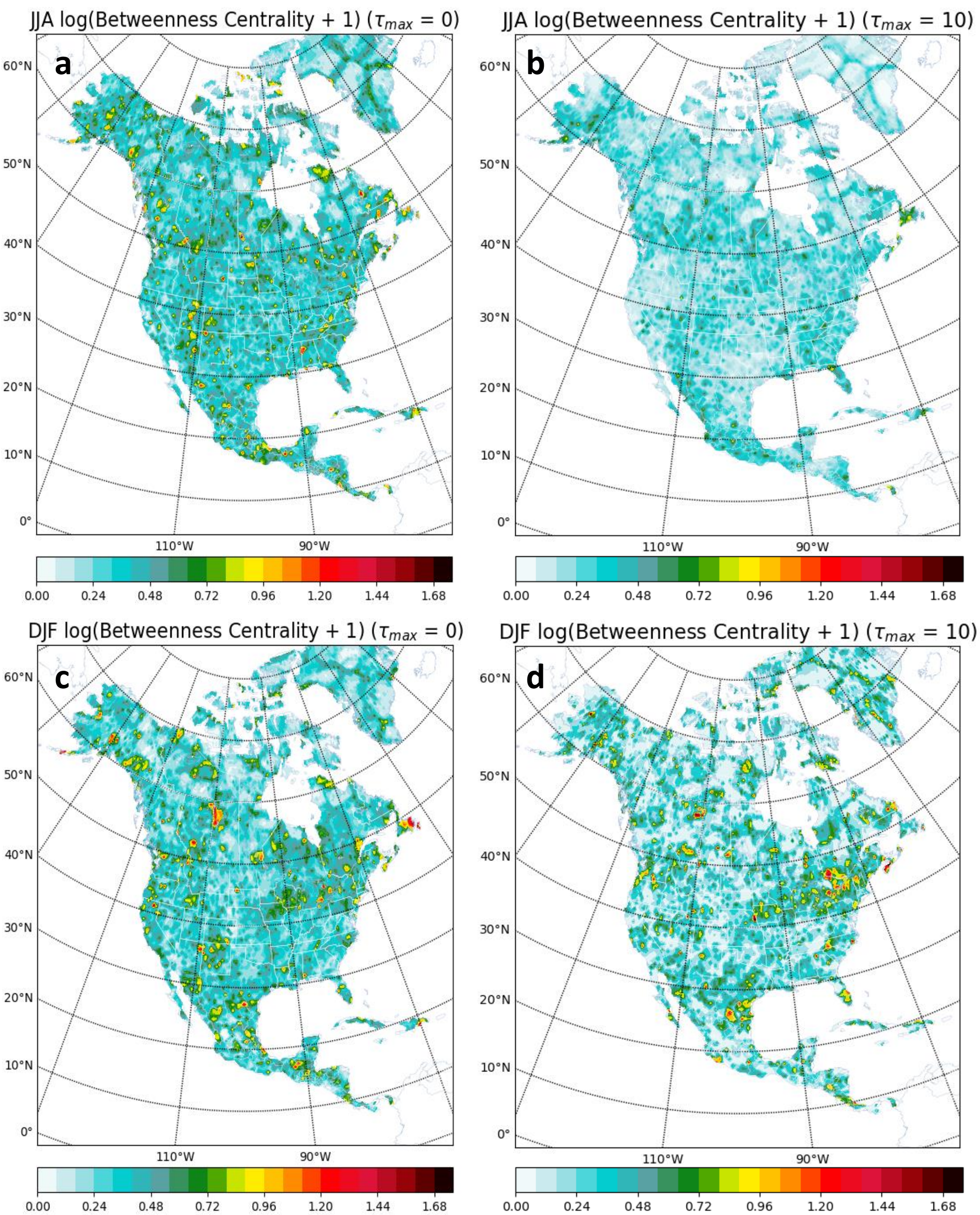

Figure 6. The maps at the top display betweenness centrality for the summer, while those at the bottom display it for the winter. In the left column are betweenness centrality maps at $\tau_{max} = 0$ day, while in the right column are those for $\tau_{max} = 10$ days.

The significance of orographic effects on the long-range transport processes of EPEs in JJA from northwest Mexico to southwest CONUS is highlighted by the area of high LRD oriented north-south between the eastern and western slopes of the Sierra Madre Occidental and the Sierra

Madre Oriental. The region of northwestern Mexico is considered the nucleus of the NAM System (Gochis et al., 2006). Our results agree with the studies of Barlow et al. (1998) and Douglas et al. (1993). They reported that at large geographical scales, the onset of the monsoon is marked by a major increase in precipitation across western Mexico, continuing northward to Arizona and New Mexico, with a corresponding reduction of precipitation over eastern Mexico and extending to Texas.

We observed a zone of moderate LRD, directed west-east, in the extratropical region, at approximately 50^0N latitude on the west coast of North America (see Fig. 7(a)). This pattern is likely related to less intense storms, which are features of the westerlies coming from the Pacific to western Canada in the summer (Tan et al., 2018). In eastern North America, however, we see many moisture pathways indicated by many regions having moderate LRD values (Fig. 7(a) and (b)). These routes are associated with hurricanes and extratropical cyclones that move from the Gulf of Mexico and the Atlantic Ocean to the eastern parts of the continent, which are transformed into EPEs by orographic features like the Saint Lawrence River basin and the Appalachian Highlands (Milrad et al., 2013). In Fig. 7(a), bands of high LRD regions can be seen above latitude 60^0N, indicating the movement of atmospheric moisture from the Arctic Ocean and the Gulf of Alaska into Alaska and northern Canada. Our findings are in line with those of (Tan et al., 2018), who used the Hybrid Single-Particle Lagrangian Integrated Trajectory to study dominant moisture pathways for extreme precipitations across Canada. Please refer to their Fig. 3 for comparison.

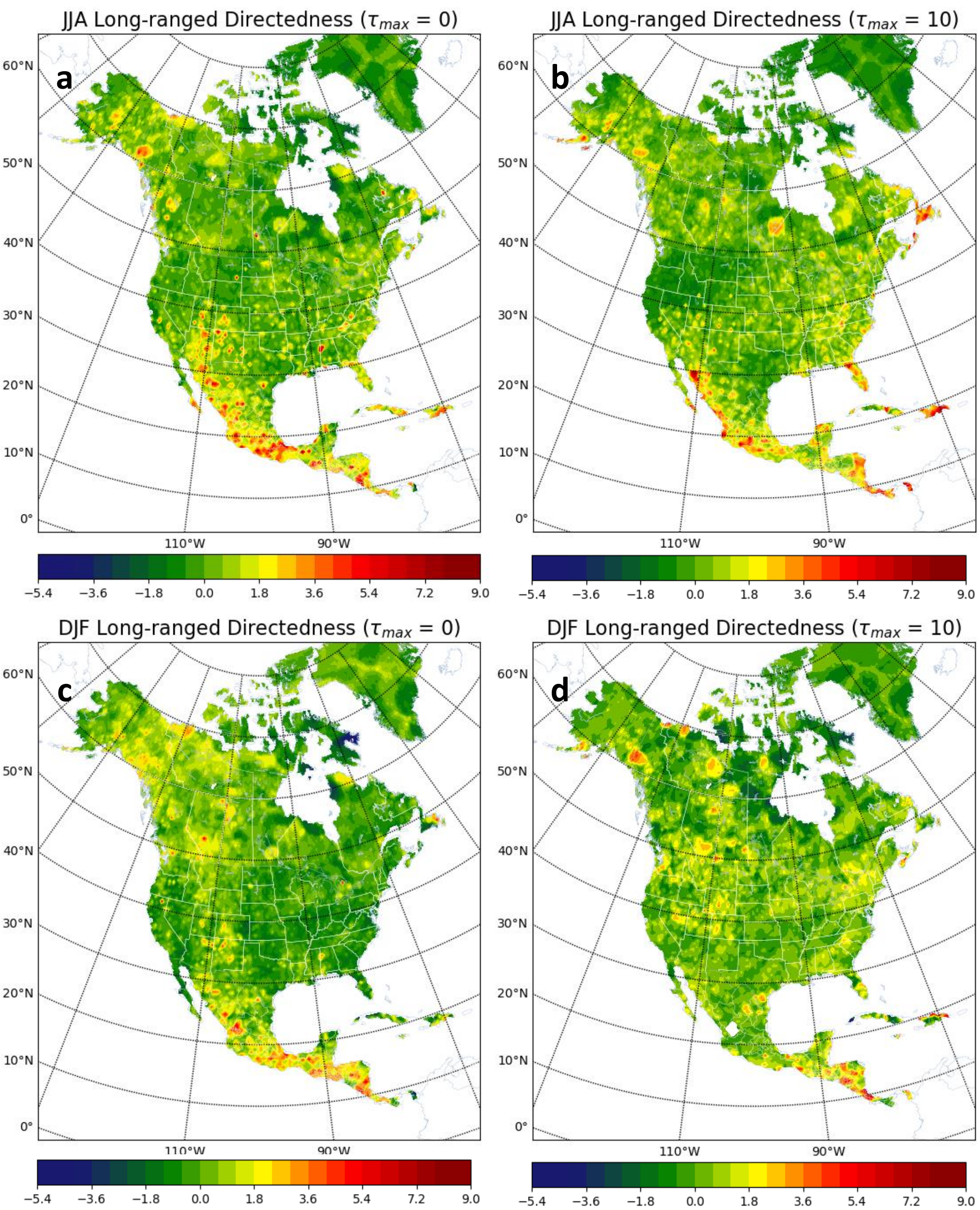

Figure 7. Long-range directedness is shown for the summer on the top maps, and for the winter on the bottom maps. Long-range directedness maps for $\boldsymbol{\tau_{max}} = 0$ days are in the left column, while those for $\boldsymbol{\tau_{max}} = 10$ days are on the right.

Figure 7(c) and (d) shows the spatial distribution of LRD during the winter season. At $\tau_{max} = 10$ days, we discovered more varied paths during the winter than during the summer (Fig. 7(d)). A long pathway runs across eastern Mexico, western Texas, and the Midwest from the tropics. We also observed a route for EPEs transport from southern Louisiana to the eastern CONUS to Quebec.

There also exists a moisture transport route from the west coast of North America, in midlatitudes, across the central to the western section of the continent (Fig. 7(d)). This implies that synoptic-scale weather systems have a more significant influence on EPEs during the winter. Our research concurs with the investigation conducted by Low et al. (2022).

According to the paths found, EPEs throughout the winter are linked to moisture carried by cyclones, anticyclones, and atmospheric rivers, among other atmospheric phenomena. The path from Louisiana to Quebec suggests that moisture is transported from the Gulf of Mexico into eastern Canada and the United States. The path intersecting the route from the west coast and the Gulf of Mexico indicates ARs feed into cyclones, as reported by Low et al. (2022).

3.3 Community detection

Community detection is an approach to grouping nodes in a network such that links inside groups are denser while links between them are sparser. Finding these communities can be useful for various purposes, such as developing a numerical prediction model for EPEs and enhancing our comprehension of the underlying mechanisms of EPEs. We used the random-walk community detection algorithm to divide the continent into sub-regions with homogeneous EPEs (Pons & Latapy, 2005). We generated 50 distinct partitions using the random-work approach and reported the mean partitions at each instant. We showed the detected communities by different colors in Fig. 8 for the JJA and DJF seasons. Figures 8(a) and 8(b) are the community detection results for the summer season. We found 10 communities in JJA $\tau_{max} = 0$. As can be seen, the detected communities roughly correspond to 1. Alaska and northwest Canada, 2. Western, central, and northern Canada, 3. Southeast Canada and northeast CONUS, 4. Southeast CONUS, 5. Mexico and south CONUS; 6. Northwest, central, and north CONUS, and south Canada; 7. Southern Greenland; 8. Northern Greenland; 9. Northern Nunavut region in Canada; and 10. Central American region.

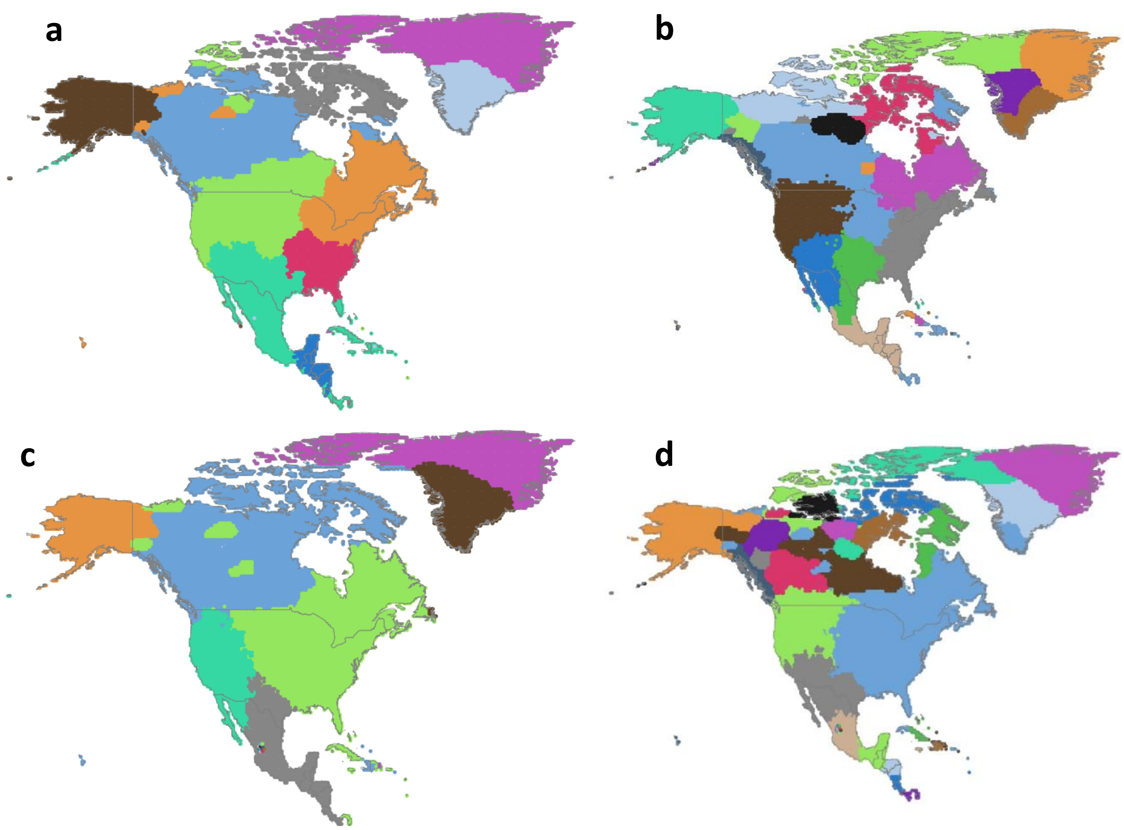

Figure 8. Communities of the EPEs networks based on the random-walk method for JJA at (a) $\tau_{max} = 0$ and (b) $\tau_{max} = 10$ days. The bottom maps show the communities detected for DJF at (c) $\tau_{max} = 0$ and (d) $\tau_{max} = 10$ days. Every community is represented with a distinct color.

At $\tau_{max} = 10$ days, we found 15 communities in the summer. On the other hand, we found seven communities in the winter $\tau_{max} = 0$ (Fig. 8c). The western coast of North America formed a sub region in DJF. We observed 16 sub regions at $\tau_{max} = 10$ days for DJF. More communities were found at longer temporal ranges than at lower range.

3.4 Climatological Interpretation

Orographic intensification of precipitation caused by the presence of the Rocky Mountains in Montana and the Canadian Rockies in Alberta makes these regions hubs for extreme precipitation propagation in the summer season. High values of DC and BC and moderate MGD and CC estimates in Montana and Alberta show that summer EPEs occurring in these regions are associated with regional precipitation systems such as localized convective cells (thunderstorms) and are transported over short distances of less than 2000 km onto neighboring regions such as the Great Plains in CONUS. The reduction in the DC values of these locations from τ_{max} = 6 days and higher further suggests that these areas are associated with short-duration extreme precipitation events, which are known to result in significant flooding (Arias et al., 2021).

In tropical and subtropical North America, however, places in Central America and northwest Mexico become hubs when EPEs occurring within 2 days and more of one another are considered for synchronization. These synchronizations in northwest Mexico and southwest CONUS are strongly associated with the North American Monsoon system (Adams & Comrie, 1997; Gochis et al., 2006; Liebmann et al., 2008b; Mechoso et al., 2012). The low CC and high MGD (above 4000 km) and LRD mean these regions are responsible for the long-distance movement of EPEs on the continent. Figure 7 (a) clearly shows the transport route of EPEs during JJA from Mexico into CONUS, the Gulf of Mexico into eastern CONUS, and from the Pacific and Arctic Ocean into Alaska and northwest Canada. The pathway from northwest Mexico into CONUS indicates that moisture responsible for EPEs comes mainly from the Gulf of Mexico and tropical North America and goes as far as west Nevada and south Idaho.

For the winter season, the hubs for EPES are located on the east coast at all τ_{max} and on the west coast at τ_{max} = 2 days and above, within the subtropical and extratropical regions. The appearance of hubs on the west coast at higher τ_{max} indicates that atmospheric rivers coming from the Pacific Ocean cause EPEs in western CONUS and southwest Canada during DJF. EPEs result from extratropical cyclones from the Atlantic Ocean in east North America. Further, fig. 5c shows that EPEs patterns are more spatial coherent on the East Coast during the winter compared to the summer, which might indicate large precipitation systems that cover more spatial area on average, dominant in the DJF. There are many intersections between EPEs pathways, as can be seen in Fig. 7 (d), which complicates dependencies in locations of extreme precipitations in the winter. Also, the longer routes for moisture transport present evidence for teleconnections related to Rossby waves and Jet streams from the southern parts of the continent to the northern regions during the winter season (Low et al., 2022).

Chapter 4 - Conclusion

The spatiotemporal patterns of extreme precipitation events (EPEs) across the continent of North America (NA) were investigated in this study using the complex network technique. We defined EPEs at a grid point (a location with a precipitation time series) using the 95th percentile of precipitation as a threshold. We then determined dependency in EPEs between any two nodes through the event synchronization (ES) method. Further, we analyzed the sensitivities of the constructed EPEs networks to a parameter of the ES method, called τ_{max}. Network measures, including degree centrality (DC), betweenness centrality (BC), clustering coefficient (CC), mean geographical distance (MGD), and long-ranged directedness (LRD) were estimated, and boundary-effect corrections were applied. We discovered hubs (grid points with high number of links) in NA based on the DC. We found hubs in places like Montana, Wyoming, Alberta, and Saskatchewan in the summer and the West Coast and the eastern NA in the winter. MGD demonstrated that northwest Mexico is involved in geographically distant connections in the summer. In the winter, the result showed that regions in McKenzie mountains, West coast, and eastern NA contributed to large spatial propagation of EPEs. Furthermore, regions participating in teleconnections and regional links were identified by MGD. An analysis of the geographic distance distribution verified the teleconnections. In particular, at $\tau_{max} = 0$ days, we discovered a crossover for the summer at 2750 km and the winter at 2200 km. We found these crossovers for the summer and winter seasons at 3150 and 2650 km, respectively, at $\tau_{max} = 10$ days.

Furthermore, through CC, we showed that EPEs are more spatially coherent in the winter season compared to the summer season across the continent. The BC result revealed specific places in Utah, Colorado, South Dakota, northern Mexico, southeast British Columbia, and northern Quebec that are important for the spatial propagation of EPEs from one region to another during the summer. While places on the West Coast, southern Colorado, New Mexico, Wisconsin, central Alberta, etc., emerged as dominant contributors during the winter. We then estimated LRD from normalized BC, CC, and MGD to uncover the transport routes of EPEs. We observed a narrow region starting at the southwestern slope of Sierra Madre Oriental and extending to Arizona, New Mexico, Utah, and Colorado, which serves as a significant pathway for transporting moisture during the summer. Whereas in winter, we found varied routes, such as pathways from eastern Mexico to western Texas to the Midwest, from the West Coast to central NA, and from Louisiana to Quebec. We identified topography as having a major influence on EPEs routes.

Based on community detection investigation, we found that the number of communities changed from summer to winter. We observed 10 for the former and 7 for the latter, showing that systems that produce larger-sized precipitation are more in winter than summer. Finally, we demonstrated that the topology of the EPEs networks depends on τ_{max}, emphasizing the importance of considering its value relative to the atmospheric phenomena of interest. The results of this study revealed synchronization patterns of EPEs across North America that can advance our understanding of intricate relationships and interdependencies between various watersheds and precipitation patterns. These insights can be applied to hydrological modeling to enhance the forecasting of hydrologic and climatic occurrences, facilitate the management of water systems, and enhance the prediction of high-impact climate-related hazards. This is particularly beneficial when combined with artificial intelligence approaches.

References

Adams, D. K., & Comrie, A. C. (1997). The North American Monsoon. *Bulletin of the American Meteorological Society*, *78*(10), 2197–2213.

Arias, P., Bellouin, N., Coppola, E., Jones, R., Krinner, G., Marotzke, J., Naik, V., Palmer, M., Plattner, G. K., Rogelj, J., & Rojas, M. (2021). *Climate Change 2021: the physical science basis. Contribution of Working Group I to the Sixth Assessment Report of the Intergovernmental Panel on Climate Change; technical summary*.

Banerjee, A., Kemter, M., Goswami, B., Merz, B., Kurths, J., & Marwan, N. (2023). Spatial coherence patterns of extreme winter precipitation in the U.S. *Theoretical and Applied Climatology*, *152*(1–2), 385–395. https://doi.org/10.1007/s00704-023-04393-5

Barlow, M., Nigam, S., & Berbery, E. H. (1998). Evolution of the North American Monsoon System. *Journal of Climate*, *11*(9).

Boers, N., Bookhagen, B., Marwan, N., Kurths, J., & Marengo, J. (2013). Complex networks identify spatial patterns of extreme rainfall events of the South American Monsoon System. *Geophysical Research Letters*, *40*(16), 4386–4392. https://doi.org/10.1002/grl.50681

Boers, N., Donner, R. V., Bookhagen, B., & Kurths, J. (2015). Complex network analysis helps to identify impacts of the El Niño Southern Oscillation on moisture divergence in South America. *Climate Dynamics*, *45*(3–4), 619–632. https://doi.org/10.1007/s00382-014-2265-7

Boers, N., Goswami, B., Rheinwalt, A., Bookhagen, B., Hoskins, B., & Kurths, J. (2019). Complex networks reveal global pattern of extreme-rainfall teleconnections. *Nature*, *566*(7744), 373–377. https://doi.org/10.1038/s41586-018-0872-x

Boers, N., Rheinwalt, A., Bookhagen, B., Barbosa, H. M. J., Marwan, N., Marengo, J., & Kurths, J. (2014). The South American rainfall dipole: A complex network analysis of extreme events. *Geophysical Research Letters*, *41*(20), 7397–7405. https://doi.org/10.1002/2014GL061829

Chen, M., Shi, W., Xie, P., Silva, V. B. S., Kousky, V. E., Higgins, R. W., & Janowiak, J. E. (2008). Assessing objective techniques for gauge-based analyses of global daily precipitation. *Journal of Geophysical Research Atmospheres*, *113*(4). https://doi.org/10.1029/2007JD009132

De Meo, P., Ferrara, E., Fiumara, G., & Provetti, A. (2011). *Generalized Louvain method for community detection in large networks*.

Dickinson, T. A., Richman, M. B., & Furtado, J. C. (2021). Subseasonal-to-Seasonal Extreme Precipitation Events in the Contiguous United States: Generation of a Database and Climatology. *Journal of Climate*, *34*(18). https://doi.org/10.1175/JCLI-D-20

Douglas, M. W., Maddox, R. A., Howard, K., & Reyes, S. (1993). The Mexican monsoon. *Journal of Climate*, *6*, 1665–1677.

Easterling, D. R., Evans, J. L., Ya Groisman, P., Karl, T. R., Kunkel, K. E., & Ambenje, P. (2000). Observed Variability and Trends in Extreme Climate Events: A Brief Review*. *Bulletin of the American Meteorological Society*, *81*(3), 417–425. https://doi.org/https:/doi.org/10.1175/1520-0477(2000)081<0417:OVATIE>2.3.CO;2

Feldstein, S. B., & Franzke, C. L. E. (2017). Atmospheric teleconnection patterns. In *Nonlinear and Stochastic Climate Dynamics* (pp. 54–104). Cambridge University Press. https://doi.org/10.1017/9781316339251.004

Fischer, E. M., & Knutti, R. (2016). Observed heavy precipitation increase confirms theory and early models. In *Nature Climate Change* (Vol. 6, Issue 11, pp. 986–991). Nature Publishing Group. https://doi.org/10.1038/nclimate3110

Gandin, L. (1965). Objective analysis of meteorological fields: Gidrometeorologicheskoe Izdatel'stvo (GIMIZ), Leningrad. *Translated by Israel Program for Scientific Translations, Jerusalem*.

Gershunov, A., Shulgina, T., Clemesha, R. E. S., Guirguis, K., Pierce, D. W., Dettinger, M. D., Lavers, D. A., Cayan, D. R., Polade, S. D., Kalansky, J., & Ralph, F. M. (2019). Precipitation regime change in Western North America: The role of Atmospheric Rivers. *Scientific Reports*, *9*(1). https://doi.org/10.1038/s41598-019-46169-w

Gershunov, A., Shulgina, T., Ralph, F. M., Lavers, D. A., & Rutz, J. J. (2017). Assessing the climate-scale variability of atmospheric rivers affecting western North America. *Geophysical Research Letters*, *44*(15), 7900–7908. https://doi.org/10.1002/2017GL074175

Gimeno, L., Nieto, R., Vázquez, M., & Lavers, D. A. (2014). Atmospheric rivers: A mini-review. In *Frontiers in Earth Science* (Vol. 2, Issue March). Frontiers Research Foundation. https://doi.org/10.3389/feart.2014.00002

Gochis, D. J., Brito-Castillo, L., & Shuttleworth, W. J. (2006). Hydroclimatology of the North American Monsoon region in northwest Mexico. *Journal of Hydrology, 316*(1–4), 53–70. https://doi.org/10.1016/j.jhydrol.2005.04.021

Gupta, S., Boers, N., Pappenberger, F., & Kurths, J. (2021). Complex network approach for detecting tropical cyclones. *Climate Dynamics*, *57*(11–12), 3355–3364. https://doi.org/10.1007/s00382-021-05871-0

Hannachi, A., Jolliffe, I. T., & Stephenson, D. B. (2007). Empirical orthogonal functions and related techniques in atmospheric science: A review. In *International Journal of Climatology* (Vol. 27, Issue 9, pp. 1119–1152). https://doi.org/10.1002/joc.1499

Houze, R. A. (2012). Orographic effects on precipitating clouds. *Reviews of Geophysics*, *50*(1). https://doi.org/10.1029/2011RG000365

Jamali, T., Ghanbarian, B., & Kurths, J. (2023). Spatiotemporal analysis of extreme precipitation events in the United States at mesoscale: Complex network theory. *Journal of Hydrology*, *627*. https://doi.org/10.1016/j.jhydrol.2023.130440

Jones, P. D., Harpham, C., Harris, I., Goodess, C. M., Burton, A., Centella-Artola, A., Taylor, M. A., Bezanilla-Morlot, A., Campbell, J. D., Stephenson, T. S., Joslyn, O., Nicholls, K., & Baur, T. (2016). Long-term trends in precipitation and temperature across the Caribbean. *International Journal of Climatology*, *36*(9), 3314–3333. https://doi.org/10.1002/joc.4557

Konapala, G., Mondal, S., & Mishra, A. (2022). Quantifying Spatial Drought Propagation Potential in North America Using Complex Network Theory. *Water Resources Research*, *58*(3). https://doi.org/10.1029/2021WR030914

Kunkel, K. E., Andsager, K., & Easterling, D. R. (1999). *Long-Term Trends in Extreme Precipitation Events over the Conterminous United States and Canada*.

Liebmann, B., Bladé, I., Bond, N. A., Gochis, D., Allured, D., & Bates, G. T. (2008a). Characteristics of North American summertime rainfall with emphasis on the monsoon. *Journal of Climate*, *21*(6), 1277–1294. https://doi.org/10.1175/2007JCLI1762.1

Liebmann, B., Bladé, I., Bond, N. A., Gochis, D., Allured, D., & Bates, G. T. (2008b). Characteristics of North American summertime rainfall with emphasis on the monsoon. *Journal of Climate*, *21*(6), 1277–1294. https://doi.org/10.1175/2007JCLI1762.1

Liu, B., Chen, J., Chen, X., Lian, Y., & Wu, L. (2013). Uncertainty in determining extreme precipitation thresholds. *Journal of Hydrology*, *503*, 233–245. https://doi.org/10.1016/j.jhydrol.2013.09.002

Liu, T., Chen, D., Yang, L., Meng, J., Wang, Z., Ludescher, J., Fan, J., Yang, S., Chen, D., Kurths, J., Chen, X., Havlin, S., & Schellnhuber, H. J. (2023). Teleconnections among tipping elements in the Earth system. *Nature Climate Change*, *13*(1), 67–74. https://doi.org/10.1038/s41558-022-01558-4

Low, Y., Gyakum, J. R., & Atallah, E. (2022). Extreme Winter Precipitation Regimes in Eastern North America: Synoptic-Scale and Thermodynamic Environments. *Monthly Weather Review*, *150*(7), 1833–1850. https://doi.org/10.1175/MWR-D-21-0255.1

Ludescher, J., Martin, M., Boers, N., Bunde, A., Ciemer, C., Fan, J., Havlin, S., Kretschmer, M., Kurths, J., Runge, J., Stolbova, V., Surovyatkina, E., & Schellnhuber, H. J. (2021). Network-based forecasting of climate phenomena. *Proceedings of the National Academy of Sciences*, *118*(47). https://doi.org/10.1073/pnas.1922872118/-/DCSupplemental

Ma, Y., & Tang, J. (2021). *Deep Learning on Graphs*. Cambridge University Press. https://doi.org/10.1017/9781108924184

Massey, F. J. (1951). The Kolmogorov-Smirnov Test for Goodness of Fit. *Journal of the American Statistical Association*, *46*(253), 68–78. https://doi.org/10.1080/01621459.1951.10500769

Mechoso, C. R., Robertson, A. W., Ropelewski, C. F., & Grimm, A. M. (2012). The Global monsoon system : research and forecast : report of the International Committee of the Third International Workshop on Monsoons (IWM-III) 2-6 November 2004, Hangzhou, China. In *World Meteorological Organization*.

Meng, X., Jia, L., & Xiang, W. (2018). Complex network model for railway timetable stability optimisation. *IET Intelligent Transport Systems*, *12*(10), 1369–1377. https://doi.org/10.1049/iet-its.2018.5257

Miller, J., & Goodrich, G. (2007). Regionalization and trends in winter precipitation in the northwestern USA. *Climate Research*, *33*, 215–227. www.int-res.com

Milrad, S. M., Atallah, E. H., & Gyakum, J. R. (2013). Precipitation Modulation by the Saint Lawrence River Valley in Association with Transitioning Tropical Cyclones*. *Weather and Forecasting*, *28*(2). https://doi.org/10.1175/WAF-D-12

Mondal, S., K. Mishra, A., Leung, R., & Cook, B. (2023). Global droughts connected by linkages between drought hubs. *Nature Communications*, *14*(1). https://doi.org/10.1038/s41467-022-35531-8

Mondal, S., Mishra, A. K., & Leung, L. R. (2020). Spatiotemporal Characteristics and Propagation of Summer Extreme Precipitation Events Over United States: A Complex Network Analysis. *Geophysical Research Letters*, *47*(15). https://doi.org/10.1029/2020GL088185

Neiman, P. J., Ola, P., Persson, G., Ralph, F. M., Jorgensen, D. P., White, A. B., & Kingsmill, D. E. (2004). Modification of Fronts and Precipitation by Coastal Blocking during an Intense Landfalling Winter Storm in Southern California: Observations during CALJET. In *MONTHLY WEATHER REVIEW* (Vol. 132).

Newman, R., & Noy, I. (2023). The global costs of extreme weather that are attributable to climate change. *Nature Communications*, *14*(1). https://doi.org/10.1038/s41467-023-41888-1

Nissen, K. M., & Ulbrich, U. (2017). Increasing frequencies and changing characteristics of heavy precipitation events threatening infrastructure in Europe under climate change. *Natural Hazards and Earth System Sciences*, *17*(7), 1177–1190. https://doi.org/10.5194/nhess-17-1177-2017

Papalexiou, S. M., & Koutsoyiannis, D. (2016). A global survey on the seasonal variation of the marginal distribution of daily precipitation. *Advances in Water Resources*, *94*, 131–145. https://doi.org/10.1016/j.advwatres.2016.05.005

Pons, P. and Latapy, M. (2005), Computing communities in large networks using random walks, LNCS 3733 - Computer and Information Sciences - ISCIS 2005. In Lecture Notes in. https://doi.org/10.48550/arXiv.physics/0512106

Quiroga, Q. R., Kreuz, T., & Grassberger, P. (2002). Event synchronization: A simple and fast method to measure synchronicity and time delay patterns. *Physical Review E - Statistical Physics, Plasmas, Fluids, and Related Interdisciplinary Topics*, *66*(4), 9. https://doi.org/10.1103/PhysRevE.66.041904

Rheinwalt, A., Marwan, N., Kurths, J., Werner, P., & Gerstengarbe, F. W. (2012). Boundary effects in network measures of spatially embedded networks. *Proceedings - 2012 SC Companion: High Performance Computing, Networking Storage and Analysis, SCC 2012*, 500–505. https://doi.org/10.1109/SC.Companion.2012.72

Shrestha, S., Fang, X., & Li, J. (2013). *Mapping the 95 th Percentile Daily Rainfall in the Contiguous U.S.*

Sun, A. Y., Xia, Y., Caldwell, T. G., & Hao, Z. (2018). Patterns of precipitation and soil moisture extremes in Texas, US: A complex network analysis. *Advances in Water Resources*, *112*, 203–213. https://doi.org/10.1016/j.advwatres.2017.12.019

Tan, X., Gan, T. Y., & Chen, Y. D. (2018). Moisture sources and pathways associated with the spatial variability of seasonal extreme precipitation over Canada. *Climate Dynamics*, *50*(1–2), 629–640. https://doi.org/10.1007/s00382-017-3630-0

Taylor, M. A., Enfield, D. B., & Chen, A. A. (2002). Influence of the tropical Atlantic versus the tropical Pacific on Caribbean rainfall. *Journal of Geophysical Research: Oceans*, *107*(9). https://doi.org/10.1029/2001jc001097

Traag, V. A., Waltman, L., & van Eck, N. J. (2019). From Louvain to Leiden: guaranteeing well-connected communities. *Scientific Reports*, *9*(1). https://doi.org/10.1038/s41598-019-41695-z

Trenberth, K. E. (2011). Changes in precipitation with climate change. *Climate Research*, *47*(1–2), 123–138. https://doi.org/10.3354/cr00953

Trenberth, K. E., Dai, A., Rasmussen, R. M., & Parsons, D. B. (2003). *The Changing Character of Precipitation*.

Vallejo-Bernal, S. M., Wolf, F., Boers, N., Traxl, D., Marwan, N., & Kurths, J. (2023). The role of atmospheric rivers in the distribution of heavy precipitation events over North America. *Hydrology and Earth System Sciences*, *27*(14), 2645–2660. https://doi.org/10.5194/hess-27-2645-2023

Viale, M., Houze, R. A., & Rasmussen, K. L. (2013). Upstream orographic enhancement of a narrow cold-frontal rainband approaching the Andes. *Monthly Weather Review*, *141*(5), 1708–1730. https://doi.org/10.1175/MWR-D-12-00138.1

Xie, P., Chen, M., & Shi, W. (2010). *CPC unified gauge-based analysis of global daily precipitation*. https://ams.confex.com/ams/90annual/techprogram/paper_163676.htm

Yang, Y., & Wu, R. (2019). Seasonal variation of precipitation over the Indochina Peninsula and its impact on the South China Sea spring warming. *International Journal of Climatology*, *39*(3), 1618–1633. https://doi.org/10.1002/joc.5904

Yuan, J., & Miller, R. L. (2002). Seasonal variation in precipitation patterns to the global ocean: An analysis of the GPCP version 2 data set. *Global Biogeochemical Cycles*, *16*(4), 50-1-50–10. https://doi.org/10.1029/2001gb001458

Zhu, Y., & Newell, R. E. (1994). Atmospheric rivers and bombs. *Geophysical Research Letters*, *21*(18), 1999–2002. https://doi.org/10.1029/94GL01710

Appendix A - **Supplementary Materials**

We provided the visual analytics for the network measures described in section 2.3 of the main text. These network measures include (1) Degree centrality (DC), (2) Mean geographical distance (MGD), (3) Clustering coefficient (CC), (4) Betweenness centrality (BC), (5) Long-ranged directedness (LRD), and (6) Community detection (CD). For each measure, maps for both summer and winter seasons are given, and all τ_{max} considered (Figures 9 - 20). That is, $\tau_{max} = 0,1,2,4,6$, and 20 days. In each figure given, plots for $\tau_{max} = 0,1,2,4,6$, and 20 days are given accordingly in subfigure (a) to (g). Also, histogram plots fare provided for the probability density function of the distance distributions of links. In addition, tables showing P-values from the Kolmogorov-Smirnov tests (KS test) (Massey, 1951) and T-tests on the distributions at different τ_{max} per measure are provided (Table 3 – 10).

Hubs (grid locations connected to many other locations on the continent) are found in Washington, Montana, and Alberta areas, among others in the summer. The hubs shifted to the East Coast in the winter. At τ_{max} = 4 days in the winter, places on the West Coast become hubs in the EPEs network through τ_{max} = 20 days.

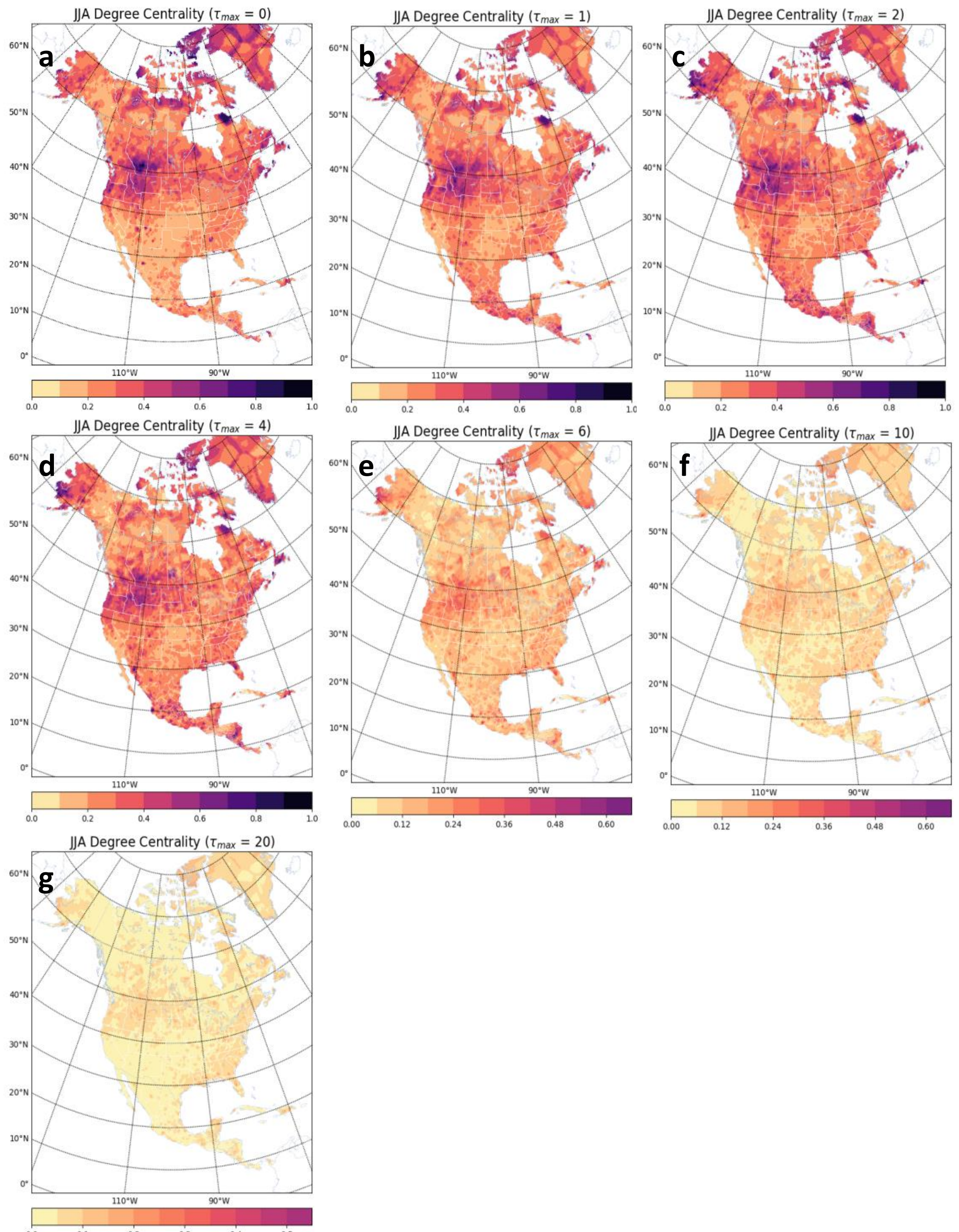

Figure 9. North American maps of degree centrality for the summer season. Results at $\tau_{max} = 1,2,4,6,$ and 20 days are accordingly arranged from (a) to (g). Some locations in Washington, Idaho, Oregon, Montana, and Alberta are hubs at $\tau_{max} = 0 – 4$ days. These places are relatively well connected compared to most areas on the continent at $\tau_{max} = 6$, 10, and 20 days.

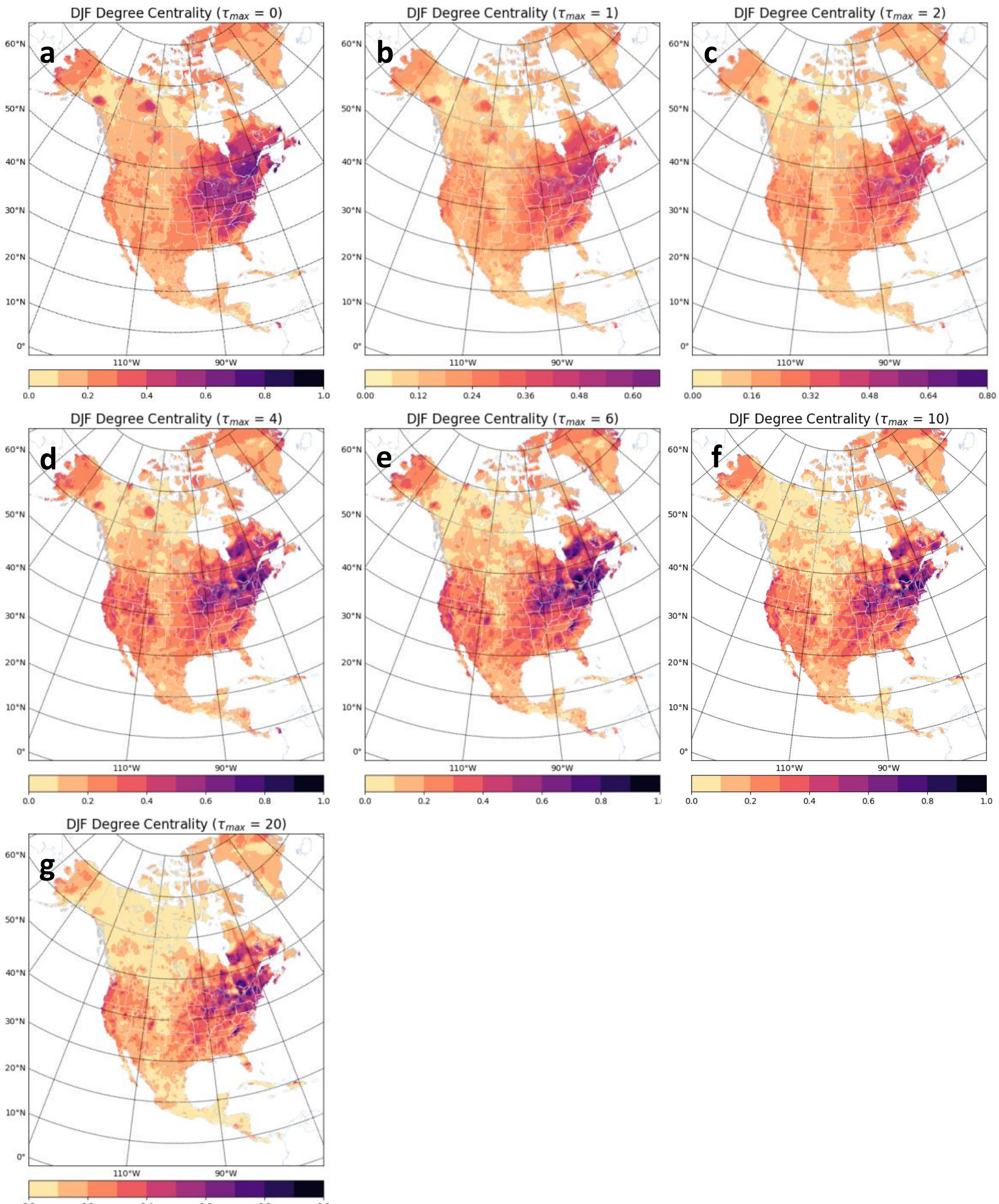

Figure 10. Maps showing degree centrality distribution across North America for the winter seasons at various τ_{max}. Many areas on the East Coast are hubs at all τ_{max}. However, places on the West Coast emerged as hubs at τ_{max} = 4 days. These patterns may be due to the atmospheric river timelines dominating the West Coast during the winter.

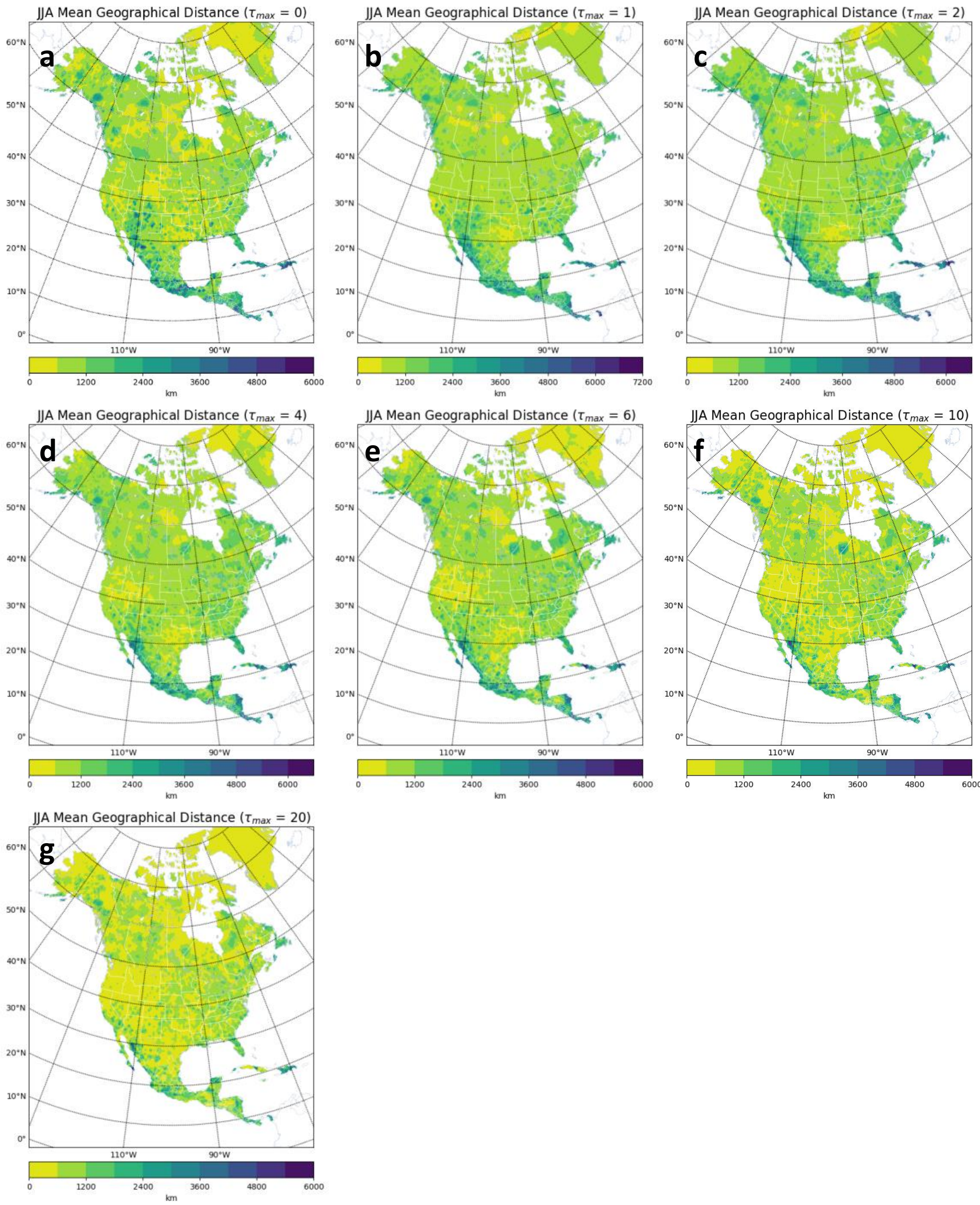

Figure 11. Maps displaying the distribution of mean geographical distance at different τ_{max} for North America's summer season.

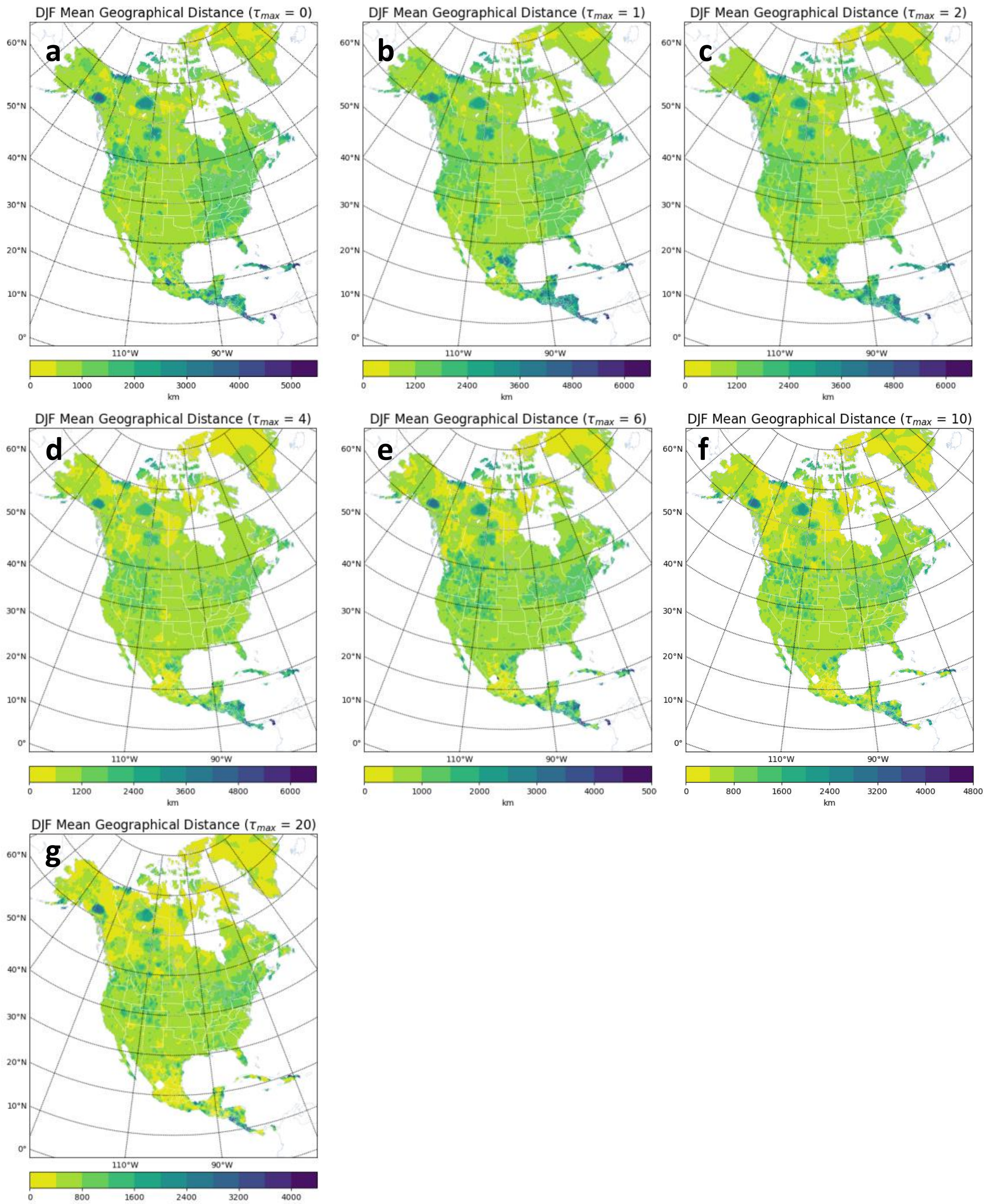

Figure 12. Maps of North America display the mean geographical distance distribution during the winter. Fewer areas contribute to the long-distance EPEs dynamic at higher τ_{max}, specifically at τ_{max} = 6 days and above.

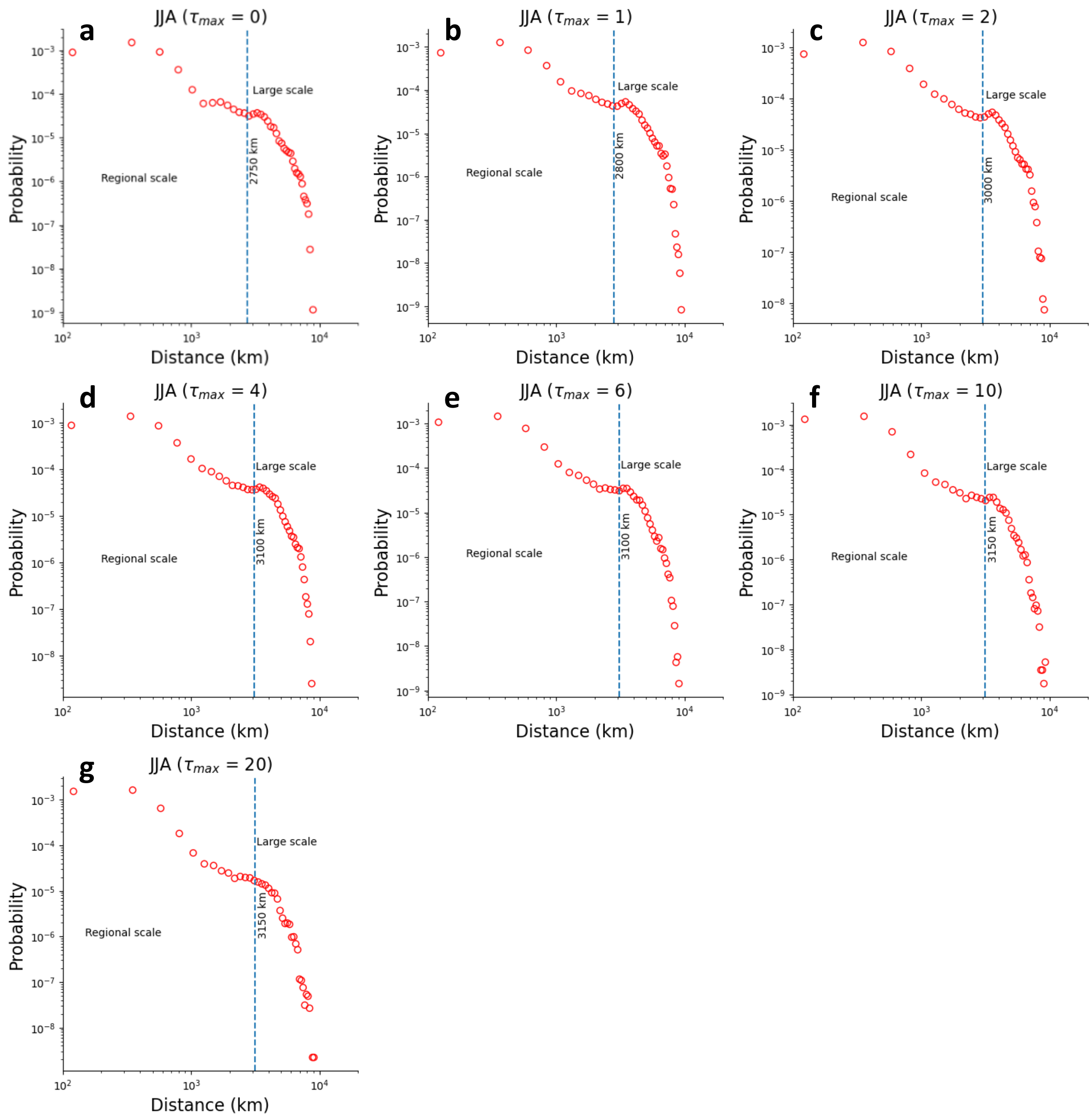

Figure 13. The probability density function of link distances during the summer season. The blue lines represent cross-over distances between the links involved in regional weather systems and those in large-scale precipitation systems.

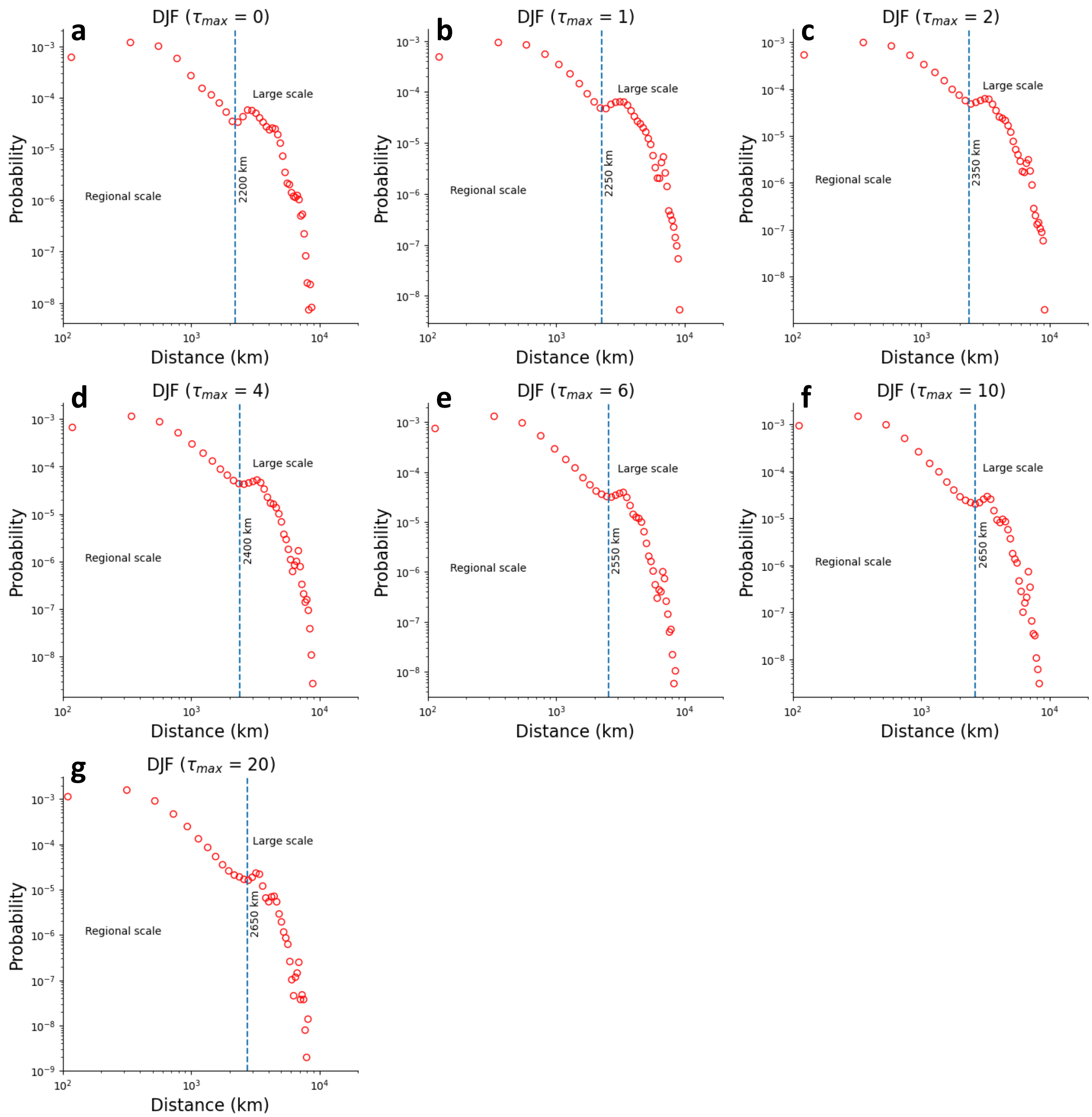

Figure 14. The wintertime probability density function of link distances. The blue lines show the cross-over distances between the links in large-scale precipitation systems and those in regional weather systems.

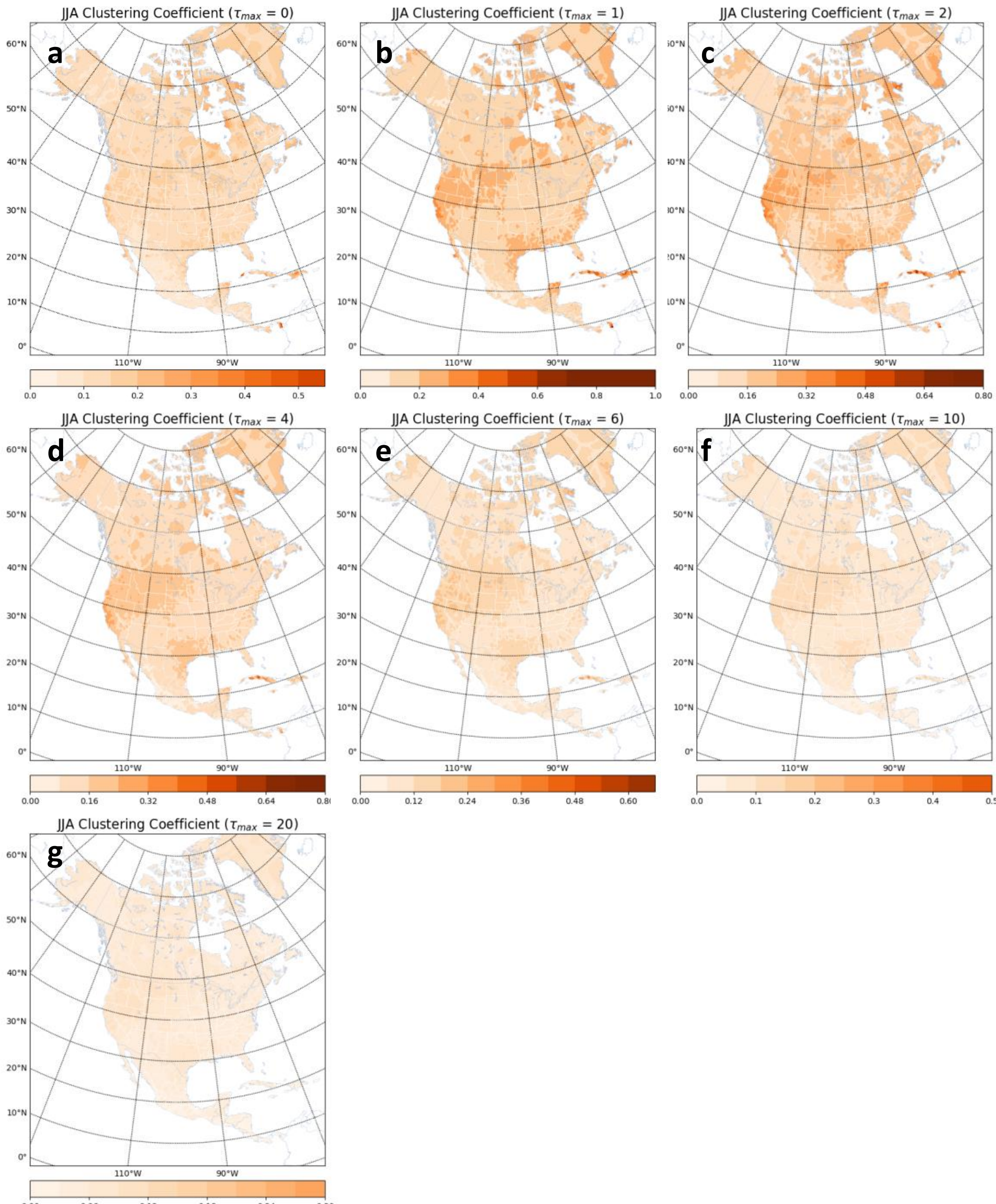

Figure 15. The maps showing the clustering coefficients over the summertime continental area of North America. When events one to two days apart are considered for synchronization, some West Coast regions show spatial coherence in EPEs.

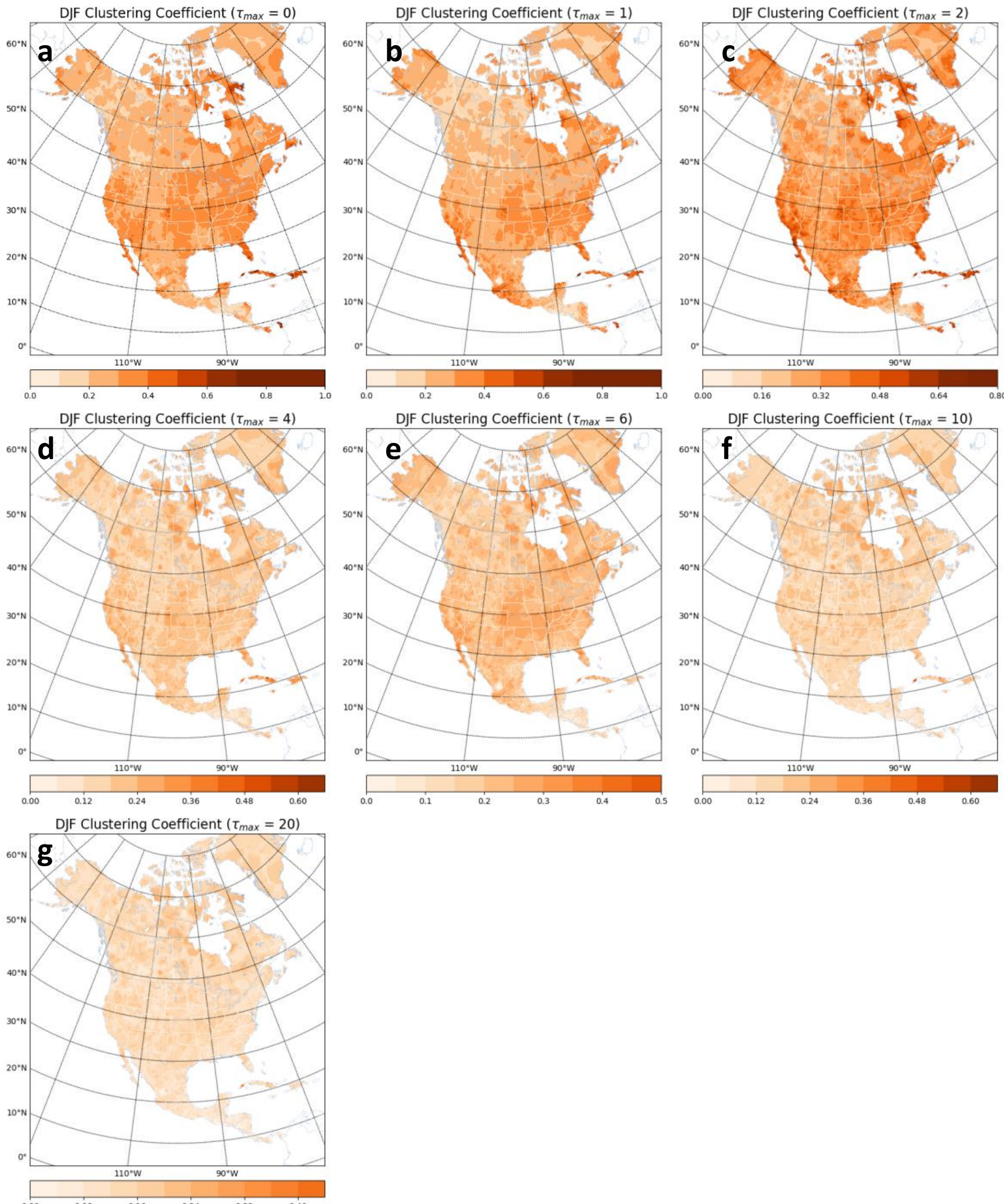

Figure 16. The maps indicating the wintertime clustering coefficients over the continent of North America. There are more EPEs spatially coherent regions in the winter than in the summer (see Figure 15).

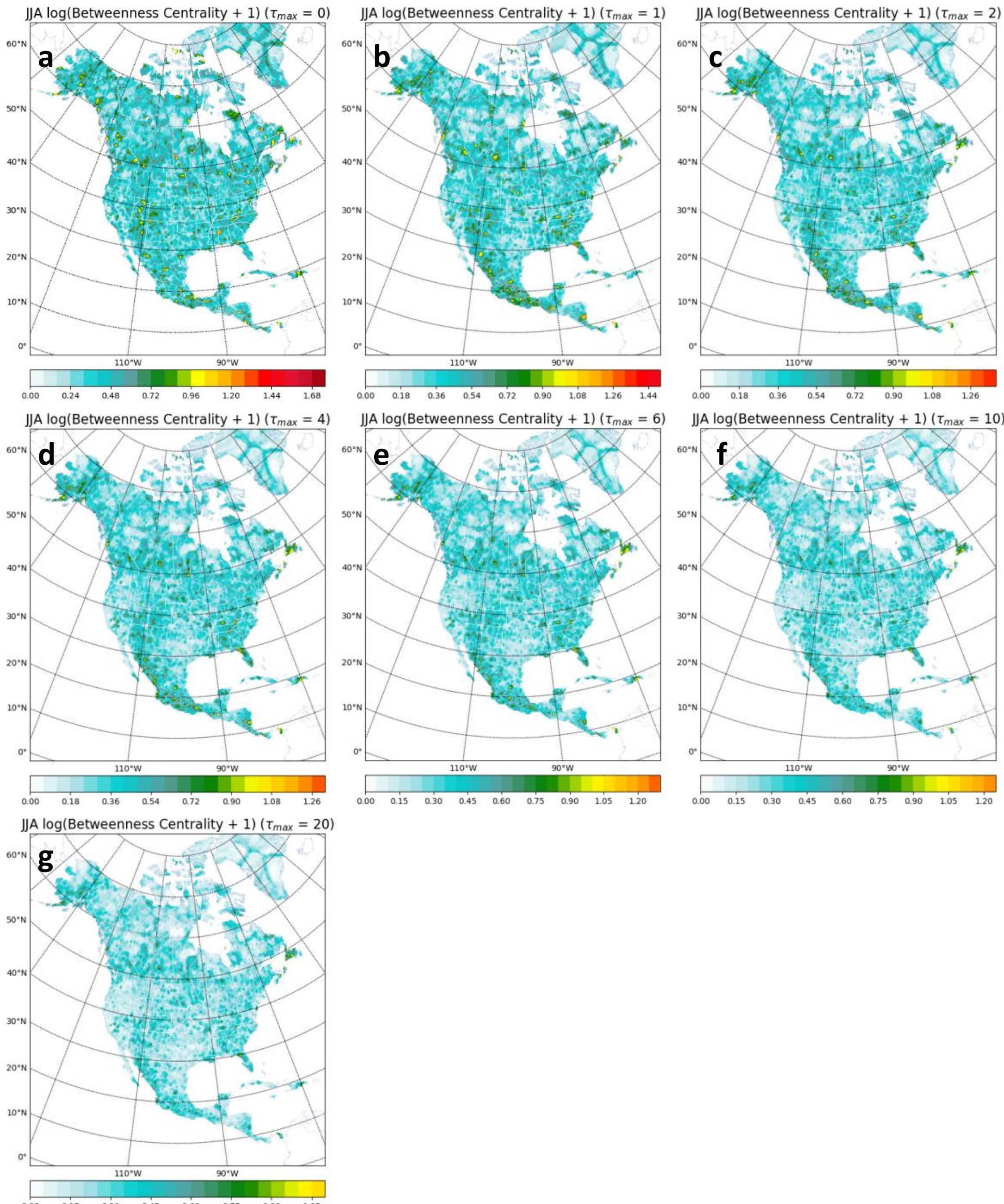

Figure 17. Maps displaying the distribution of the betweenness centrality values during the summer season in North America. More places contributed to broadcasting EPEs at lower τ_{max}, i.e., 0, 1, 2, and 4 days, than at higher τ_{max}.

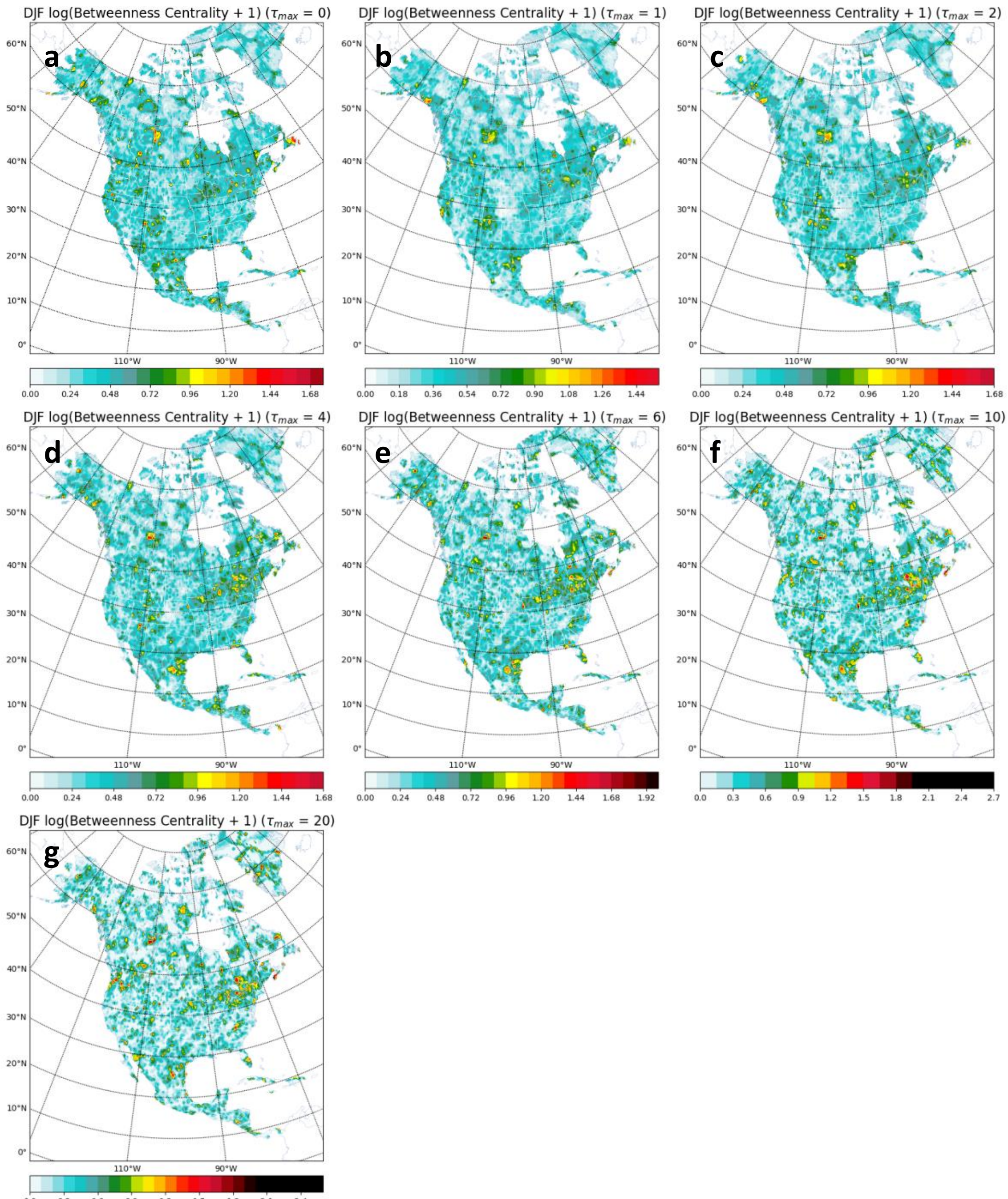

Figure 18. Maps showing how betweenness centrality values are distributed in North America during the winter season. The number of areas involved in transferring EPEs across regions on the continent generally increases with τ_{max} during the winter.

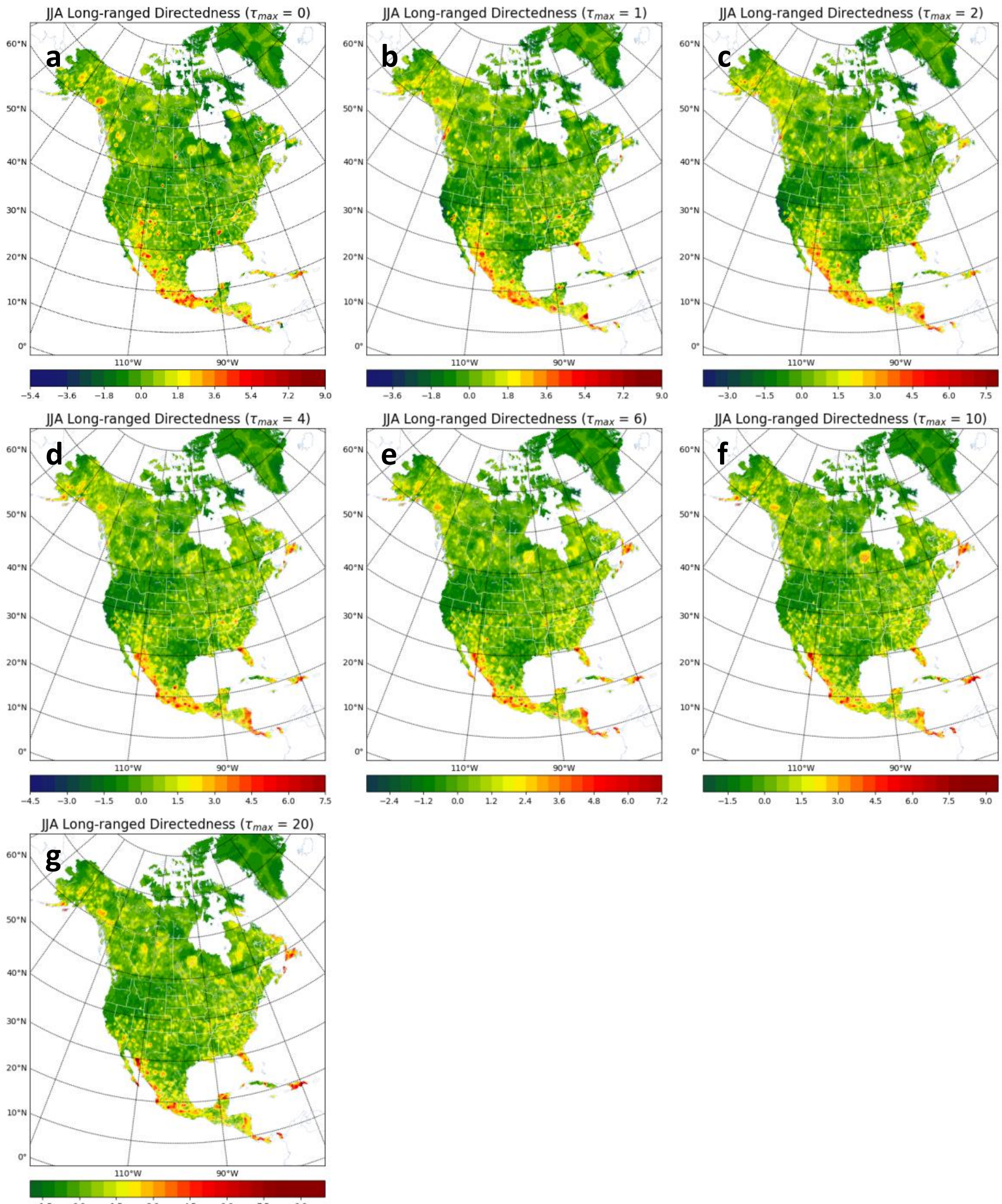

Figure 19. Long-range directedness (LRD) maps of North America during the summer. EPEs are anticipated to feature directed moisture transfer mechanisms over narrow transport channels and large spatial scales in areas with high LRD values. A narrow rope-like region from Central America through northwest Mexico into the southwest CONUS exhibits high LRD values at every τ_{max} considered.

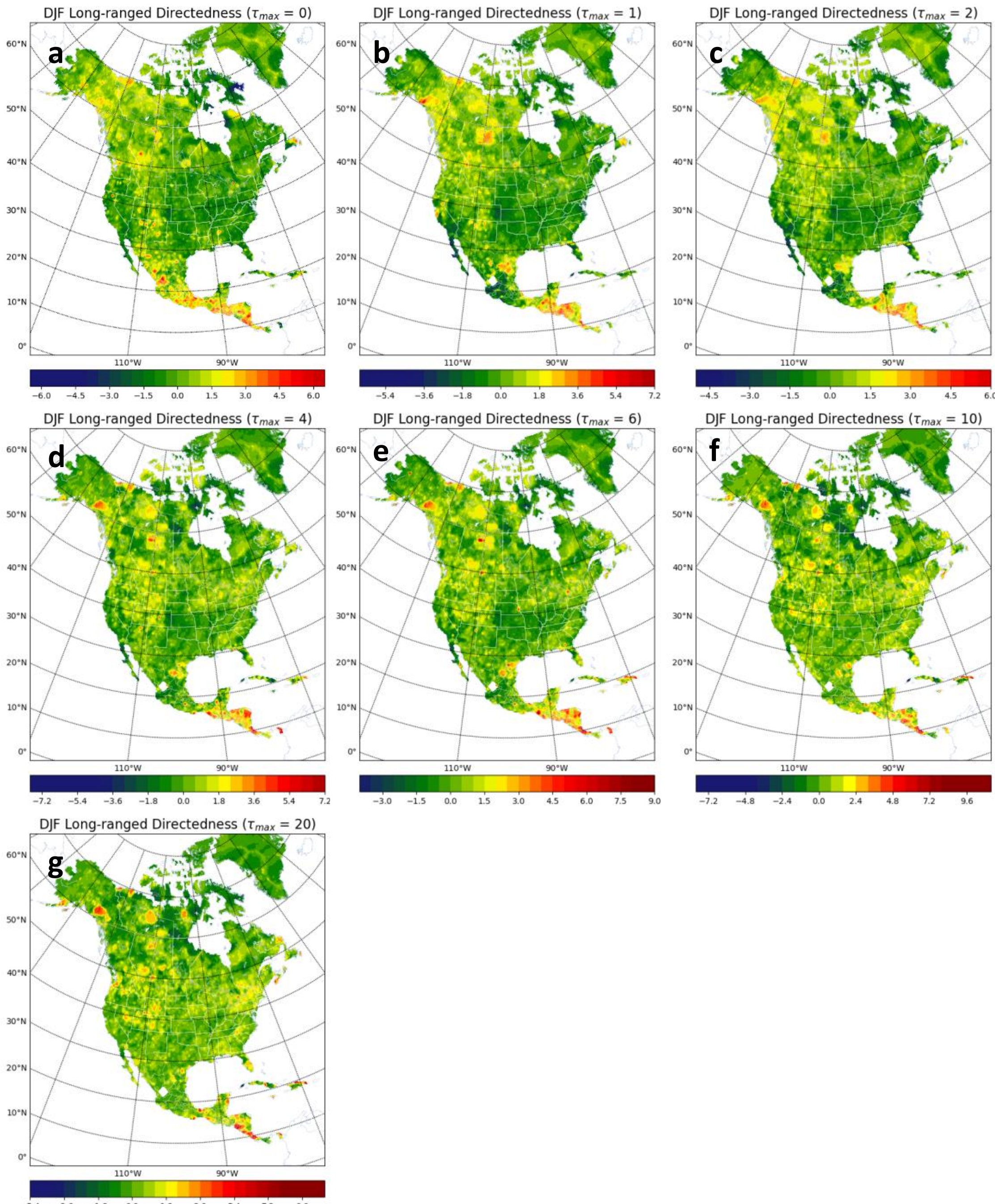

Figure 20. Maps showing long-range directedness (LRD) throughout North America over the winter. High LRD estimates are found for a route from northeast Alaska, across Canada to the East Coast, which is probably connected to jet streams, starting at τ_{max} = 4 days.

Table 3. P-values from Paired T-tests for DC distributions at different τ_{max} in the summer season. The null hypothesis is that collections of DC at two τ_{max} have the same mean at 0.05 significant level.

	τ_{max} 0	τ_{max} 1	τ_{max} 2	τ_{max} 4	τ_{max} 6	τ_{max} 10	τ_{max} 20
τ_{max} 0		0.0000	<0.0001	<0.0001	0.0000	0.0000	0.0000
τ_{max} 1			<0.0001	<0.0001	0.0000	0.0000	0.0000
τ_{max} 2				0.0000	0.0000	0.0000	0.0000
τ_{max} 4					0.0000	0.0000	0.0000
τ_{max} 6						0.0000	0.0000
τ_{max} 10							0.0000

Table 4. P-values from Paired T-tests for DC distributions at different τ_{max} in the winter season. The null hypothesis is that collections of DC at two τ_{max} have the same mean at 0.05 significant level.

	τ_{max} 0	τ_{max} 1	τ_{max} 2	τ_{max} 4	τ_{max} 6	τ_{max} 10	τ_{max} 20
τ_{max} 0		0.0000	0.0000	<0.0001	0.0700	0.0000	0.0000
τ_{max} 1			0.0000	<0.0001	0.0000	<0.0001	0.0000
τ_{max} 2				0.0000	0.0000	0.0000	<0.0001
τ_{max} 4					<0.0001	0.0000	0.0000
τ_{max} 6						0.0000	0.0000
τ_{max} 10							0.0000

Table 5. P-values from KS testing for mean geographical distance (MGD) distributions at different τ_{max} in the summer season. At the 0.05 significant level, collections of MGD at two τ_{max} are taken from the same probability distribution, according to the null hypothesis.

	τ_{max} 0	τ_{max} 1	τ_{max} 2	τ_{max} 4	τ_{max} 6	τ_{max} 10	τ_{max} 20
τ_{max} 0		0.0000	0.0000	<0.0001	<0.0001	0.0000	0.0000
τ_{max} 1			<0.0001	<0.0001	0.0000	<0.0001	0.0000
τ_{max} 2				0.0000	0.0000	0.0000	0.0000
τ_{max} 4					<0.0001	0.0000	0.0000
τ_{max} 6						<0.0001	0.0000
τ_{max} 10							<0.0001

Table 6. P-values from KS testing for winter mean geographical distance (MGD) distributions at various τ_{max}. Collections of MGD at two τ_{max} are drawn from the same probability distribution, according to the null hypothesis, at the 0.05 significant level.

	τ_{max} 0	τ_{max} 1	τ_{max} 2	τ_{max} 4	τ_{max} 6	τ_{max} 10	τ_{max} 20
τ_{max} 0		0.0000	0.0000	<0.0001	<0.0001	0.0000	0.0000
τ_{max} 1			<0.0001	0.0000	0.0000	0.0000	0.0000
τ_{max} 2				<0.0001	0.0000	0.0000	0.0000
τ_{max} 4					<0.0001	0.0000	0.0000
τ_{max} 6						<0.0001	0.0000
τ_{max} 10							<0.0001

Table 7. P-values from KS clustering coefficient (CC) distributions in North America at different τ_{max} in the summer season.

	τ_{max} 0	τ_{max} 1	τ_{max} 2	τ_{max} 4	τ_{max} 6	τ_{max} 10	τ_{max} 20
τ_{max} 0		0.0000	0.0000	<0.0001	0.0000	0.0000	0.0000
τ_{max} 1			<0.0001	0.0000	0.0000	0.0000	0.0000
τ_{max} 2				0.0000	0.0000	0.0000	0.0000
τ_{max} 4					0.0000	0.0000	0.0000
τ_{max} 6						0.0000	0.0000
τ_{max} 10							0.0000

Table 8. P-values from KS clustering coefficient (CC) distributions in North America at different τ_{max} during the winter season.

	τ_{max} 0	τ_{max} 1	τ_{max} 2	τ_{max} 4	τ_{max} 6	τ_{max} 10	τ_{max} 20
τ_{max} 0		0.0000	<0.0001	0.0000	0.0000	0.0000	0.0000
τ_{max} 1			0.0000	0.0000	0.0000	0.0000	0.0000
τ_{max} 2				0.0000	0.0000	0.0000	0.0000
τ_{max} 4					0.0000	0.0000	0.0000
τ_{max} 6						0.0000	0.0000
τ_{max} 10							0.0000

Table 9. P-values from Paired T-tests for CC distributions at different τ_{max} in JJA. The null hypothesis is that collections of CC at two τ_{max} have the same mean at 0.05 significant level.

	τ_{max} 0	τ_{max} 1	τ_{max} 2	τ_{max} 4	τ_{max} 6	τ_{max} 10	τ_{max} 20
τ_{max} 0		0.0000	0.0000	<0.0001	0.0000	0.0000	0.0000
τ_{max} 1			<0.0001	0.0000	0.0000	0.0000	0.0000
τ_{max} 2				0.0000	0.0000	0.0000	0.0000
τ_{max} 4					0.0000	0.0000	0.0000
τ_{max} 6						0.0000	0.0000
τ_{max} 10							0.0000

Table 10. P-values for CC distributions at various τ_{max} during DJF from Paired T-tests at the 0.05 significant level.

	τ_{max} 0	τ_{max} 1	τ_{max} 2	τ_{max} 4	τ_{max} 6	τ_{max} 10	τ_{max} 20
τ_{max} 0		0.0000	0.0000	0.0000	0.0000	0.0000	0.0000
τ_{max} 1			0.0000	0.0000	0.0000	0.0000	0.0000
τ_{max} 2				0.0000	0.0000	0.0000	0.0000
τ_{max} 4					0.0000	0.0000	0.0000
τ_{max} 6						0.0000	0.0000
τ_{max} 10							0.0000